UNIVERSITY OF HELSINKI REPORT SERIES IN ASTRONOMY

No. 20

Magnetic Phenomena of the Interstellar Medium in Theory and Observation

Miikka Väisälä

Academic dissertation

Department of Physics
Faculty of Science
University of Helsinki
Helsinki, Finland

To be presented, with the permission of the Faculty of Science of the University of Helsinki, for public criticism in the University of Helsinki Main building (Fabianinkatu 33), Auditorium XII, on November 1st 2017, at 12 o'clock noon.

Helsinki 2017

Cover picture: A synthetic map of polarization angle dispersion $\mathcal{S}$ with $R_{\max} = 1\,\mathrm{kpc}$, based on the results of *Paper VI*.

ISSN 1799-3024 (print version)
ISBN 978-951-51-2777-8 (print version)
Helsinki 2017
Helsinki University Print (Unigrafia)

ISSN 1799-3032 (pdf version)
ISBN 978-951-51-2778-5 (pdf version)
ISSN-L 1799-3024
http://ethesis.helsinki.fi/
Helsinki 2017
Electronic Publications @ University of Helsinki
(Helsingin yliopiston verkkojulkaisut)

Miikka Väisälä: **Magnetic Phenomena of the Interstellar Medium in Theory and Observation**, University of Helsinki, 2017, 68 p. + appendices, University of Helsinki Report Series in Astronomy, No. 20, ISSN 1799-3024 (print version), ISBN 978-951-51-2777-8 (print version), ISSN 1799-3032 (pdf version), ISBN 978-951-51-2778-5 (pdf version), ISSN-L 1799-3024

Keywords: magnetohydrodynamics, interstellar medium, galactic dynamo, polarization, star formation, GPGPU

Abstract

Magnetic fields and turbulent flows pervade the interstellar medium on all scales. The magnetic turbulence that emerges on the large scales cascades towards the small scales where it influences molecular cloud structure, and star formation within the densest and coldest clumps of the clouds. Active star formation results in supernovae, and the supernova-driven turbulence takes part in the galactic dynamo process leading to the inverse cascade of turbulent energy. Such a process is one example of self-organisatory processes in the interstellar medium where order arises from chaos.

Supernovae also induce and influence other important processes in the galactic disks, and this thesis examines some of them. Differentially rotating disk systems, such as galaxies, are prone to magnetorotational instability, where weak magnetic fields destabilise the otherwise hydrodynamically stable disk system, and lead to angular momentum transport outwards. However, magnetorotational instability can be quenched or even damped by another source of turbulence such as supernovae. As both magnetorotational instability and supernovae are capable of producing dynamo effects, the galactic large-scale magnetic fields are proposed to arise as an interplay of these two effects. In addition, supernovae are observed to be able to generate and sustain large-scale flows in galaxies through the anisotropic kinetic α effect.

Thermodynamical effects have a significant influence on the properties of turbulence. Due to baroclinicity, the supernova-driven turbulence is highly vortical in nature. These types of flows produce a narrow, non-Gaussian velocity distribution with extended wings and an exponential magnetic field distribution. Such effects should be taken into account when interstellar turbulence is parametrized in the form of initial conditions and forcing functions for the purpose of making smaller scale models of molecular cloud formation. The Gaussianity of the magnetic field fluctuations is a common assumption, for example, when fitting magnetic field models to explain large-scale polarization maps of the interstellar dust, and our results suggest that such assumptions should require more examination.

To study these phenomena, a combination of numerical approaches and observational methods are needed. Exploring physics of turbulence requires the tools of high-performance computing and precise, high-order numerical schemes. Because of the rapidly increasing demands of computation, novel approaches have to be investigated. To improve computational efficiency this thesis shows how the sixth-order finite difference method can

be accelerated with the help of graphics processing units.

The properties of the interstellar medium can be examined best by the emission of atomic/molecular gas and by the emission, absorption and scattering of interstellar dust. Looking at small-scale phenomena, molecular line emission from cold prestellar cores is explored. More large-scale effects are examined with the help of polarized dust emission, by combining radiative transfer calculations with the results of a supernova-driven model of the interstellar medium, including a realistic multiphase structure and dynamo-generated small- and large-scale magnetic fields.

This thesis contains seven papers. Of these, three papers examine the processes driving turbulence in differentially rotating disks via numerical modelling, while one paper looks into how graphics processing units can accelerate such calculations. Observationally, two papers study cold cores and early stages of star formation with the help of radio telescopes, and one paper examines how supernova-driven turbulence is reflected in the large-scale emission of diffuse interstellar dust.

Acknowledgements

I wish to thank my supervisors Dr. Maarit Käpylä (Aalto University/MPS), Dr. Jorma Harju (University of Helsinki) and Dr. Mika Juvela (University of Helsinki) for their guidance over the years. Your combined presence has allowed me to look into the subject of my study from multiple different directions. I am particularly grateful to Maarit, as her active and supportive approach to research has encouraged me to continue until this point. I also appreciate the work and feedback of the pre-examiners, Dr. Katia Ferrière (CNRS, Observatoire Midi-pyrénées) and Dr. Tobias Heinemann (Københavns Universitet). In addition, I wish to thank Dr. Mordecai-Mark Mac Low (Columbia University/American Museum of Natural History) for acting as the Opponent and Prof. Karri Muinonen as the Custos.

While the majority of the work has been done in the Department of Physics in the University of Helsinki, a number of short and long research visits have played an important part in the process. For those, I wish to thank Nordita in Stockholm, Max Planck Institute for Solar System Research in Göttingen and Department of Computer Science in the Aalto University in Espoo for their hospitality. Especially, my various visits to Nordita over the years, already first time as an undergraduate, have provided inspiration to kick start my involvement with magnetohydrodynamics. Also, my visit to MPS was critically important in the last moments of thesis writing.

A number of my colleagues and collaborators require special recognition. I wish to thank Dr. Frederick Gent for numerous scientific discussions, which frequently helped me to clear up my often complicated mind, and also for helping with the English language with this manuscript. Johannes Pekkilä has been invaluable as a working partner with the Astaroth code development, and I wish him well with his upcoming academic career. Prof. Axel Brandenburg has provided me various inspiration as a scientist, and I thank him for pushing me forward, both knowingly and unknowingly. Last but not least, my thanks to Dr. Petri Käpylä, Dr. Dhrubaditya Mitra, Dr. Malcolm Walmsley, Dr. Matthias Rheinhardt, Dr. Thomas Hackman, Dr. Omer Anjum and Dr. Olli Sipilä for collaboration, discussions and/or other such matters.

Lastly, I am grateful for my parents Pekka and Seija, and my brothers Iiro and Juuso for many things. Also my friends – Henri, Arto, Bar-chè, Mé-sèl, Santeri, Maria, Agnieszka, Kira, Aleksi, Essi, and others – have been there to keep some sanity in my life during this long, and sometimes frustratingly difficult, project, and for that I am very grateful.

I would like to thank the financial support from the Jenny and Antti Wihuri Foundation, the Finnish Cultural Foundation, the Magnus Ehrnrooth Foundation, the University of Helsinki and the Academy of Finland. Financial support from the Academy of Finland ReSoLVE Center of Excellence (grant No. 272157) is acknowledged. The majority of the simulations featured in this thesis were performed using the supercomputers hosted by the CSC – IT Center for Science Ltd. in Espoo, Finland, which is administered by the Finnish Ministry of Education.

List of publications

Paper I: M.J. Korpi, P.J. Käpylä, **M.S. Väisälä**, 2010, *"Influence of Ohmic diffusion on the excitation and dynamics of MRI"*, Astronomische Nachrichten, 331, No. 1, 34-45

Paper II: J. Ruoskanen, J. Harju, M. Juvela, O. Miettinen, A. Liljeström, **M. Väisälä**, T. Lunttila, S. Kontinen, 2011, *"Mapping the prestellar core Ophiuchus D (L1696A) in ammonia"*, Astronomy & Astrophysics, 534, A122

Paper III: M.S. Väisälä, J. Harju, M.J. Mantere, O. Miettinen, R.S. Sault, C.M. Walmsley, J.B. Whiteoak, 2014, *"High-resolution ammonia mapping of the very young protostellar core Chamaeleon-MMS1"*, Astronomy & Astrophysics, 564, A99

Paper IV: M.S. Väisälä, A. Brandenburg, D. Mitra, P.J. Käpylä, M.J. Mantere, 2014, *"Quantifying the effect of turbulent magnetic diffusion on the growth rate of the magneto-rotational instability"*, Astronomy & Astrophysics, 567, A139

Paper V: J. Pekkilä, **M.S. Väisälä**, M.J. Käpylä, P.J. Käpylä, O. Anjum, 2017, *"Methods for compressible fluid simulation on GPUs using high-order finite differences"*, Computer Physics Communications, 217, 11-22

Paper VI: M.S. Väisälä, F.A. Gent, M. Juvela, M.J. Käpylä, 2017, *"The supernova-regulated ISM. IV. A comparison of simulated polarization with Planck observations"*, Astronomy & Astrophysics, Submitted for publication

Paper VII: M.J. Käpylä, F.A. Gent, **M.S. Väisälä**, G.R. Sarson, 2017, *"The supernova-regulated ISM. III. Generation of vorticity, helicity and mean flows"*, Astronomy & Astrophysics, Submitted for publication

List of abbreviations

AKA	Anisotropic kinetic α
AMR	Adaptive mesh refinement
API	Application programming interface
ATCA	Australian Telescope Compact Array
BE	Bonnor-Ebert
CPU	Central processing unit
CFL	Courant-Friedrich-Levy
DNS	Direct numerical simulation
FDM	Finite difference method
FHSC	First hydrostatic core
FOSA	First-order smoothing approximation
GMC	Giant molecular clouds
GPGPU	General-purpose computing on graphics processing units
GPU	Graphics processing unit
HD	Hydrodynamics
HPC	High-performance computing
ISM	Interstellar medium
LOS	Line of sight
LTE	Local thermodynamic equilibrium
LSD	Large-scale dynamo
POS	Plane of sky
MHD	Magnetohydrodynamics
MPI	Message passing interface
PAH	Polycyclic aromatic hydrocarbon
SED	Spectral energy distribution
SSD	Small-scale dynamo
SN	Supernova
VeLLO	Very low luminosity object

Contents

1 Introduction

The interstellar medium (ISM) is a blanket term for essentially any type of matter that can be found between stars. It is a wide concept, comprising a multitude of phenomena, ranging from galactic scale down to the level of particle physics. The focus of this thesis is in the dynamics and magnetic fields of the ISM, descending down from the kiloparsec scales of our Milky Way galaxy down to the AU scales of star formation.

1.1 Composition of the ISM

The ISM consists of two major component substances, gas and dust, which as such are highly generalized categories. "Gas" simply refers to any kind of molecular and atomic matter, and "dust" to any small particles bigger than simple molecules, from nearly molecular sized polycyclic aromatic hydrocarbons (PAHs) to fine grains of dust that would be visible to the human eye. Table 1.1 depicts some aspects of the gaseous ISM. Most of the volume is taken by the hot and warm diffuse gas. Within it, there are cold and dense molecular clouds, containing in themselves dense clumps and cores, where star formation occurs.

Hydrogen is naturally the most abundant element in the universe. Using the scaling of Lodders (2003), the solar system elemental abundances for the ten most common elements are

Element	H	He	O	C	Ne
A(El)	12	10.984 ± 0.02	8.76 ± 0.05	8.46 ± 0.04	7.95 ± 0.10
Element	N	Mg	Si	Fe	S
A(El)	7.90 ± 0.11	7.62 ± 0.02	7.61 ± 0.02	7.54 ± 0.03	7.26 ± 0.04

where $A(\mathrm{El}) = \log\left[n(\mathrm{El})/n(\mathrm{H})\right] + 12$ is a logarithmic scaling comparison to the abundance of H. All these elements can be found, in some form or another, in the ISM as gas or dust.

The gaseous ISM is partially ionized. This is induced by a number of energetic processes, such as heating by supernova (SN) shocks, stellar radiation and the collisions of cosmic ray particles (Elmegreen & Scalo, 2004; Bergin & Tafalla, 2007). Particularly visible are the HII regions, which are created by high-energy radiation from the massive OB stars (e.g. Hester et al., 1996). Because of the partial ionization of the ISM, there are dynamically significant magnetic fields present. Due to their dynamical importance, magnetic fields take part in many processes in the ISM, such as star formation. However,

Component	T (K)	n (cm^{-3})	f	Example
Hot ionized	$\sim 10^6$	~ 0.0065	$0.6 - 0.7$	SN-driven hot gas
Warm ionized	~ 8000	$0.2 - 0.5$	$0.1 - 0.23$	HII regions
Warm atomic	$6000 - 10000$	$0.2 - 0.5$	0.2	Diffuse HI
Cold atomic	$50 - 100$	$20 - 50$	$0.02 - 0.04$	Cold HI clouds
Molecular	$10 - 20$	$10^2 - 10^6$	$5 \cdot 10^{-4}$	Molecular clouds (H_2)
$\hookrightarrow$ Clouds	≈ 10	$50 - 500$		Taurus, Oph, Musca
$\hookrightarrow$ Clumps	$10 - 20$	$10^3 - 10^4$		B213, L1709
$\hookrightarrow$ Cores	$8 - 12$	$10^4 - 10^5$		L1544, L1498, B68

Table 1.1: Properties of diffuse ISM and cold molecular clouds, clumps and cores, where T is temperature, n hydrogen number density and f volume filling factor. Values adapted from Ferrière (2001, Table 1) with additions from Bergin & Tafalla (2007, for molecular clouds) and (Korpi, 1999, for the range of f).

it is especially challenging to study the magnetic fields, as they are not directly observable (Beck, 2016).

Observing interstellar dust provides another window to explore the ISM. The dust density directly reflects the general density of the ISM, as the dust-to-gas ratio in the Milky Way is roughly in the order of 10^{-2}. However, the exact estimates can be sensitive to the assumptions of dust composition (Zubko et al., 2004), and can vary with physical conditions and metallicity in some galaxies (e.g. Parkin et al., 2012). The exact material composition of the cosmic dust is uncertain, but there are reasonable candidate materials for the bulk of the ISM, the largest category being, mostly amorphous, silicates (Draine, 2003).

The dust itself can be observed by its absorption, scattering and emission (Steinacker et al., 2013). It is easiest to detect absorption and scattering due to dust with short wavelengths such as optical and near-infrared, while the thermal emission of dust becomes visible in far-infrared and sub-millimetre bands. In recent years the dust continuum emission has gained increasing importance, as the combination of the ESA *Planck* satellite and the *Herschel Space Observatory* has produced a sizable amount of new observational data on the interstellar dust emission (e.g. Planck Collaboration XI, 2014; Juvela et al., 2011).

In the scope of this thesis, dust is of particular interest due to its polarized thermal emission (Pelkonen et al., 2009). The dust grains are sensitive to the magnetic fields, which affect their alignment (Draine & Weingartner, 1996; Ward-Thompson et al., 2000; Andersson et al., 2015). This is reflected in the polarization of their emitted light, which can be used to estimate the plane-of-sky (POS) structure of the magnetic field in the ISM. It is of particular interest that the *Planck* satellite mission has provided an extensive all-sky map of the dust polarization in our Galaxy (Planck Collaboration Int. XIX, 2015), making the exploration of large-scale magnetic effects easier.

1.2 Magnetic turbulence

The ISM is highly turbulent, and as it is partially ionized, this turbulence is magnetic by nature. Turbulent flows are characterized by chaotic changes in pressure and flow velocity, and the presence of the magnetic field complicates matters even further by adding additional forces to the flow.

Turbulent systems are usually described with hydrodynamic and magnetic Reynolds numbers,

$$\mathrm{Re} = \frac{UL}{\nu} \quad \text{and} \quad \mathrm{Re}_M = \frac{UL}{\eta}, \tag{1.1}$$

respectively where U and L are the characteristic velocities and length scales of the examined system, and ν and η are the respective kinematic and magnetic diffusivities. For fully ionized ISM, these values are enormously high with $\mathrm{Re} = 5 \times 10^9$ and $\mathrm{Re}_M = 3 \times 10^8$ (Korpi, 1999).

Interstellar turbulence gains energy from various processes. Some of the turbulence can be caused by shearing stresses connected to galactic differential rotation. Shear is an especially powerful source of turbulence when acting together with a weak magnetic field through magnetorotational instability (MRI) (Velikhov, 1959; Chandrasekhar, 1960; Balbus & Hawley, 1991; Hawley & Balbus, 1991), where the shearing tension induced by rotation to the magnetic field is a driving force for turbulence.

Rotational and gravitational energies of the Galaxy are not the only contributors to ISM turbulence. The most powerful source is the energy input from the stars. The energy of supernovae (SNe) is by orders of magnitude stronger than any other effects (e.g. Abbott, 1982; Korpi, 1999). This implies that any realistic model of interstellar turbulence should consider the stellar forcing, either directly by modelling it, or indirectly by parametrizing it – such as by trying to forge a suitable forcing function.

Turbulence is relevant on all scales, and it is connected across all scales. If there is energy driving a turbulent process on the large scales, then the majority of the energy will cascade to smaller scales. These small-scale phenomena affect the large scales, for example, through star formation resulting in SNe. They, in turn, will drive turbulence in the presence of rotationally induced anisotropy, that is known to lead to a dynamo instability, that can lead to the generation of large-scale magnetic fields from small-scale motions – a type of phenomenon also called an inverse cascade (Meneguzzi et al., 1981; Balsara & Pouquet, 1999; Brandenburg, 2001).

Therefore, to understand how magnetic field influences processes like star formation, in the long run, it is important to understand the whole energy spectrum of magnetohydrodynamic (MHD) turbulence. While a molecular cloud which fulfils the Jeans criteria will eventually form a star, star formation efficiency, accretion disk dynamics and protostellar outflows will be affected by the nature of the initial magnetic field and how it has been induced. This acts as an overarching motivation in this thesis when connecting large- and medium-/small-scale MHD phenomena.

1.3 Importance of numerical modelling

Due to the magnetic nature of the ISM, the equations of magnetohydrodynamics (MHD) are often utilized in modelling its behaviour. With an MHD description, it is conveniently possible to describe ionized plasma as a magnetized compressible fluid. The word "fluid" refers to a description of amorphous medium such as gas and liquid, which on large scales behaves like a continuous unit. This is possible,because the average mean free path of a single particle in the fluid is much shorter than the examined scale. In that case, the fluid is dominated by the particle collisions which then manifest themselves as collective behaviour. While MHD is a highly functional approximation when its criteria are fulfilled, there are alternative descriptions of plasma, like the full kinetic description. However, the computational costs of such approach can get excessive, unless focused on a very restricted problem (e.g. von Alfthan et al., 2014).

MHD equations are highly nonlinear. It is possible to model MHD with analytical tools, such as mean field methods (Rädler, 1980), but in practice exploring most problems requires a numerical approach. The popular methods for doing so include finite difference methods (see e.g. the introduction by Brandenburg, 2003), finite-volume methods (e.g. Gressel et al., 2008; Käppeli & Mishra, 2016) and spectral methods (e.g. Hirshman & Whitson, 1983). Here the focus is on the finite difference method (FDM), which has been utilized in all MHD simulations performed in connection with this thesis. FDM requires spatial and temporal discretization of the system of equations being examined. Spatial derivatives are calculated by approximating them over stencils of chosen order (precision). For example, a 6th-order stencil uses three adjacent points on the either side of the point along the direction, in which the derivative is computed (see e.g. Fig. 1 in *Paper V*). High-order stencils are desirable, as they can better handle sudden changes, if proper attention is given to the numerical viscosity schemes, such as SN shocks (Brandenburg, 2003; Haugen et al., 2004).

Discretization of vector operations is affected by the choice of the domain (compare e.g. Cartesian vs. spherical grids), although transformations between different types of grids can be applied, as done in many multiphysics codes, such as Pencil Code. Grid sizes attainable with the current high-performance computing clusters are of order $(10^3)^3$ to $(10^4)^3$, whilst most simulations remain below $(10^3)^3$. Ideally, one desires as high resolution as possible to any given problem, but any numerical setup will encounter limits with both memory and processing power. Adding physics, such as extra variables, increasing domain size or resolution, and adding time iterations can all increase computing time and memory consumption beyond acceptable limits (see Fig. 2.1).

Numerical MHD generally requires the tools of high-performance computing (HPC). Typically, tasks are divided across multiple processor nodes in parallel, utilizing the message passing interface (MPI), to reduce the time required for the calculations. Even if the problem and the chosen solver would allow the time saving to scale perfectly as the number of processing elements grows, the grid size sets a limit for the scalability. When the data to be communicated becomes large relative to the size of the data array being computed, time savings are no longer obtained. Therefore, improving computational

capacity has to be approached in other ways. In addition, as computing centres grow, energy efficiency of normal processors becomes an issue (Mittal & Vetter, 2014).

One possibility is to accelerate computation with graphics processing units (GPU). GPUs are parallel processors which are able to compute several simultaneous floating-point operations quickly. This makes them faster in performance to normal CPU which function in a serial fashion. However, the efficiency must be traded off against flexibility, and utilizing GPUs requires consideration of bespoke computational problems. General-purpose computing on graphics processing units (GPGPU) is a relatively recent development. The original use of GPUs has been to process computer graphics with high efficiency, but such application programming interfaces (API) as CUDA and OpenCL now allow the use of GPUs for alternative tasks. GPUs are particularly well suited to computationally bound tasks such as FDM, where several floating-point operations are calculated repeatedly. The efficiency may also be reflected in the energy savings, which can be significant on big computing cluster facilities (Mittal & Vetter, 2014).

Unfortunately, utilizing GPUs for scientific computing is far from straightforward. The most difficult aspect is programming the practical implementations. As the GPU device is a separate entity from the hosting central processing unit (CPU), communication between these two must be taken into account – being mindful of the high latency in communication between the host and the device. When programming with GPUs, the code has to be able to handle both CPU and GPU, and in addition, the memory management of GPU will require particular attention to avoid losing any potential gain in performance, as our results point out in *Paper V*. All these aspects together make it challenging to optimize the code and computational method. Developing computational capacity is the key to improving computational MHD in general, so a part of this thesis discusses improving performance through GPUs. To explore this, we have developed the Astaroth code, which utilizes CUDA to calculate 6th-order finite differences.

This thesis is organized as follows. Chapter 2 introduces issues relating to numerical MHD computation and potential solutions available through GPUs. Chapter 3 discusses central observational methods connected to the presented articles. Chapter 4 considers ISM turbulence in galactic disks. Chapter 5 explores the smaller scales of cold cores. Chapter 6 relates MHD modelling to observations through simulated polarization. Chapter 7 describes the papers included in this thesis, and Chapter 8 concludes the thesis with a look into future directions.

2 Numerical magnetohydrodynamics

MHD is a discipline of science, which studies magnetized fluids. MHD is important for astrophysics because practically all fluids of interest have dynamically influential magnetic fields. For fluids to be magnetized, partial ionization is required, which is common in many astrophysical systems, such as in stars, space weather, the ISM and in various accretion disks. In essence, MHD couples the equations of fluid dynamics/hydrodynamics (HD) with Maxwell's equations, and therefore many of the essential methods are already utilized in the HD domain. In astrophysical environments, fluid/plasma is compressible, consisting of strongly turbulent gas with very high Reynolds numbers.

A benefit of the MHD method is its flexibility, sufficiently complex to account for a substantial part of the physical forces, while simple enough to be reasonably calculable on modern computers. Therefore, MHD simulations are widely used in ISM studies; such as simulations of Gent et al. (2013a,b) featured in *Paper VI*. An alternative approach to plasma propagation would be the kinetic interpretation with Vlasov equations, but in such a case computational requirements become even more intense, imposing more limited and specialized scope for the simulations (see e.g. von Alfthan et al., 2014).

A specialised class of numerical models are required to examine MHD problems, and there are numerous choices of numerical methods available. One such method is finite difference method (FDM), which has been utilized in all of the papers in this thesis featuring fluid simulations. The basic principles of FDM are straightforward; in a sense that it describes derivatives of partial differential equations with simple arithmetric operations. However, it is not possible to avoid complications which arise from both numerical stability issues and required processing power. Therefore, the first half of this chapter discusses methods and issues connected to MHD computations with FDM, and why high-order numerical schemes are important when dealing with turbulence simulations. In addition, the second half shines some light on accelerating FDM with GPUs, where the method development has resulted in the experimental code, Astaroth, to function as a practical proof of concept concerning the GPU implementation.

2.1 Equations of magnetohydrodynamics

MHD is an approximative method that requires three primary conditions to be fulfilled. First, the average of mean free path of plasma particles is sufficiently small in relation to the examined length scale. This makes the system of particles highly collisional, ap-

proaching a Maxwellian particle distribution function, and it can then be examined as a continuous fluid instead of separate particles. Second, relevant length scales are larger than the Debye length of the charged particles, and due to Debye screening, a plasma is effectively neutral when on scales much larger than the Debye length, as Coulomb interactions have most of their weight on short ranges. Third, the displacement current is neglected in the electromagnetic equations, allowing for the description of electromagnetic phenomena only with $\mathbf{B}$, in the set of MHD equations. This is reasonable when the changes in $\mathbf{E}$ are of low frequency, leading also to quasi-neutrality. However, this is an approximation and the electric field continues to be present in the system. These approximations allow for exploring electromagnetic effects combined with standard fluid dynamics in a simple compact form.

A central element of MHD is how the electromagnetism is handled. Fundamental to MHD, the induction equation can be derived from the starting point of Maxwell's equations of electromagnetism, here in cgs system of units, in connection with Ohm's law modified with the Lorentz force.

$$\begin{aligned}
\text{Gauss's law} \quad & \nabla \cdot \mathbf{E} &&= 4\pi\rho_e && \text{(I)} \\
\text{Gauss's law for magnetism} \quad & \nabla \cdot \mathbf{B} &&= 0 && \text{(II)} \\
\text{Faraday's law of induction} \quad & \nabla \times \mathbf{E} &&= -\frac{1}{c}\frac{\partial \mathbf{B}}{\partial t} && \text{(III)} \\
\text{Ampère's law} \quad & \nabla \times \mathbf{B} &&= \frac{1}{c}\left(4\pi\mathbf{j} + \frac{\partial \mathbf{E}}{\partial t}\right) && \text{(IV)} \\
\text{Ohm's law} \quad & \mathbf{j} &&= \sigma\left(\mathbf{E} + \frac{1}{c}\mathbf{u} \times \mathbf{B}\right)
\end{aligned} \tag{2.1}$$

Taking a curl of the Ohm's law and combining it with Maxwell III

$$\frac{1}{c}\frac{\partial \mathbf{B}}{\partial t} = \nabla \times \left(\frac{1}{c}\mathbf{u} \times \mathbf{B} - \mathbf{j}/\sigma\right), \tag{2.2}$$

then, utilizing Maxwell IV and setting $\frac{\partial \mathbf{E}}{\partial t} \to 0$,

$$\frac{\partial \mathbf{B}}{\partial t} = \nabla \times \left(\mathbf{u} \times \mathbf{B} - \frac{c^2}{4\pi\sigma}\nabla \times \mathbf{B}\right), \tag{2.3}$$

and applying Maxwell II, the result is the *MHD induction equation*

$$\frac{\partial \mathbf{B}}{\partial t} = \nabla \times (\mathbf{u} \times \mathbf{B}) + \eta\nabla^2\mathbf{B}, \tag{2.4}$$

where $\eta = \frac{c^2}{4\pi\sigma}$ is the magnetic diffusivity.

The hydrodynamic and magnetic Reynolds numbers, introduced in Chapter 1, describe the relative importance of the diffusive effects,

$$\mathrm{Re} = \frac{UL}{\nu} \quad \text{and} \quad \mathrm{Re}_M = \frac{UL}{\eta}, \tag{2.5}$$

The ratio of these two is presented as the magnetic Prandtl number

$$\mathrm{Pr}_M = \frac{\nu}{\eta}. \tag{2.6}$$

The Reynolds numbers are very high for the ISM, far beyond the critical Re where inertial forces are large enough to induce a turbulent state in the flow. ISM flows are also supersonic (Ma $\sim$ 1...50), and therefore susceptible to shocks. In practice, when performing numerical MHD simulations with FDM schemes, the stability depends on the strength of viscosity. Thus, Reynolds numbers must be kept unrealistically small, because the limited resolution MHD simulations will encounter issues of numerical instability with velocities too high or viscosities too low. These issues are discussed later in this chapter.

2.1.1 Expanded set of equations

In addition to the induction equation, the expanded set of equations are composed of the standard conservation laws. The MHD equations have various formulations as required by the practical considerations of the specific problem. The following presentation uses the Pencil Code[1] formulation, which is essentially utilized by all papers that deal with MHD modelling in this thesis. In the Pencil Code conservative formulation is dropped because of the overall applicability of the solved equations. For instance, $\ln \rho$ may be used, because the densities can vary several orders of magnitude. This means that the scheme does not guarantee that density and thermal, kinetic and magnetic energies are conserved. Therefore, in practice, one has to observe the diagnostic output of the simulation to spot any adverse non-conservative effects. However, non-conservative form makes it possible to use options such as logarithmic expressions for variables, which allow for a large dynamical range in density and temperature, making the non-conservative form more accurate than the conservative in some circumstances (Brandenburg, 2003).

Density is handled by the continuity equation

$$\frac{D \ln \rho}{Dt} = -\nabla \cdot \mathbf{u}, \tag{2.7}$$

where $D/Dt = \partial/\partial t + \mathbf{u} \cdot \nabla$ is the advective derivative.

The velocity field $\mathbf{u}$ is described by the momentum equation written for velocity

$$\frac{D\mathbf{u}}{Dt} = -c_s^2 \nabla \left(\frac{s}{c_p} + \ln \rho \right) + \nu \left(\nabla^2 \mathbf{u} + \frac{1}{3} \nabla (\nabla \cdot \mathbf{u}) + 2\mathbf{S} \cdot \ln \rho \right) + \frac{\mathbf{j} \times \mathbf{B}}{\rho} + \mathbf{f}, \tag{2.8}$$

with $\mathbf{f}$ being some additional added force, c_s the sound speed, and the traceless rate-of-strain tensor $\mathbf{S}$ is defined as

$$S_{ij} = \frac{1}{2} \left(\frac{\partial u_i}{\partial x_j} + \frac{\partial u_j}{\partial x_i} - \frac{2}{3} \delta_{ij} \nabla \cdot \mathbf{u} \right). \tag{2.9}$$

[1] `https://github.com/pencil-code/`, see also Pencil Code User's Manual (2017)

The thermal energy is handled by the entropy equation

$$\rho T \frac{Ds}{Dt} = \mathcal{H} - \mathcal{C} + \nabla \cdot (K \nabla T) + \eta \mu_0 \mathbf{j}^2 + 2\rho\nu \mathbf{S} \otimes \mathbf{S}, \tag{2.10}$$

featuring also $\mathcal{H}$ and $\mathcal{C}$ as heating an cooling and K is thermal conductivity. To close the system of equations, a further equation is required, such as the ideal gas equation of state,

$$p = \frac{k_\mathrm{B}}{\mu m_\mathrm{u}} \rho T, \tag{2.11}$$

where k_B represents the Boltzmann constant, m_u the atomic mass unit and μ the mean molecular weight.

The induction equation is presented in terms of the vector potential $\mathbf{A}$ ($\nabla \times \mathbf{A} = \mathbf{B}$)

$$\frac{\partial \mathbf{A}}{\partial t} = \mathbf{u} \times \mathbf{A} - \eta \mu_0 \mathbf{j}, \tag{2.12}$$

which conveniently, for numerical purposes, excludes the possibility of divergence in the $\mathbf{B}$ field.

The exact number of terms in the equations will vary in practice. Depending on the problem that is examined, different choices have to be made, which are a balance between desired physical accuracy and available computing power. In the scope of this thesis, such effects can include shearing and rotation (*Paper I*; *Paper IV*; *Paper VII*), forcing functions (*Paper I*; *Paper III*; *Paper V*), energy input from supernovae (*Paper VII*) and radiative heating and cooling (*Paper VII*).

In the full ISM simulations, differential rotation requires similar computational accuracy and virtually the same power as if it was left out. More decisive factors are the inclusion of the magnetic fields, the amount of stratification and the rate of heating from SNe. These most significantly constrain the resolution, computing timestep and number of iterations required. Whichever combination, implementation of FDM is built on simple discretized operations.

2.2 Finite difference method and its alternatives

FDM has its particular advantages and disadvantages. A specific advantage of FDM is its ease of implementation with high-order of accuracy, which is essential for accurately modelling turbulence. However, there are other alternatives to FDM used in astrophysics, namely spectral method, finite volumes method (FVM) and smoothed particle hydrodynamics (SPH).

The spectral method is the most precise (Gottlieb & Hesthaven, 2001; Kerzendorf & Sim, 2014). However, computations are slow and parallelization to multiple processors is difficult. As SPH approximates the fluid with particle representation, it is a very flexible method for problems where there are multiple length scales involved. However, due to its particle nature SPH is problematic with magnetic fields as it is prone to creating spurious divergence in the magnetic field (Tóth, 2000).

The advantage of the FVM method is that it is a conservative scheme and can be adapted more easily to exotic grid geometries (Ziegler, 2008; Balsara & Dumbser, 2015), which can be particularly useful when creating code utilizing adaptive mesh refinement (AMR). It can be significantly more complex to construct and more challenging to compute each iteration than the FDM.

No current numerical solvers are perfect. The choice of the method is therefore up to the given physical problem, practical availability of tools and researchers' familiarity with the given numerical method.

2.3 Resolving turbulence with finite difference method

The basic function of the FDM is based on approximating derivatives via the summation of neighbouring elements (for 2nd, 4th and 6th order 1st and 2nd derivatives see Table 2.1). This spatial approximation is combined with a suitable iterative time integration scheme, such as a Runge-Kutta method (see e.g, *Paper V*). Given suitable initial conditions and specified boundary conditions (Brandenburg, 2003), the system of differential equations can be solved throughout the finite modelled domain and evolved over finite time.

2nd	$f_i' =$	$(-f_{i-1} + f_{i+1})/(2\delta x)$
4th		$(f_{i-2} - 8f_{i-1} + 8f_{i+1} - f_{i+2})/(12\delta x)$
6th		$(-f_{i-3} + 9f_{i-2} - 45f_{i-1} + 45f_{i+1} - 9f_{i+2} + f_{i+3})/(60\delta x)$
2nd	$f_i'' =$	$(f_{i-1} - 2f_i + f_{i+1})/(\delta x^2)$
4th		$(-f_{i-2} + 16f_{i-1} - 30f_i + 16f_{i+1} - f_{i+2})/(12\delta x^2)$
6th		$(2f_{i-3} - 27f_{i-2} + 270f_{i-1} - 490f_i + 270f_{i+1} - 27f_{i+2} + 2f_{i+3})/(180\delta x^2)$

Table 2.1: 2th, 4th and 6th order finite difference derivatives for values f at the point i (Brandenburg, 2003). Truncation errors are proportional to powers of the grid separation length (δx^2, δx^4 or δx^6 in each order). Only even numbered orders are used, because odd numbered orders are susceptible to diffusive errors.

When discretizing the system into a grid, values are assumed for relevant physical variables at specified points on the grid, beginning with a set of initial values and applying the relevant boundary conditions. The equations are non-dimensionalized as computers cannot interpret unit properties, only the variables' numerical values. Therefore, the system can be described with respect to key non-dimensional parameters. Characteristic physical scales specific to the problem are factored out. When modelling turbulence, one seeks to understand how each non-dimensional parameter affects the onset of turbulence and its properties. For example, in *Paper IV* the growth of the turbulence in examined through by varying the parameters of differential rotation, shear and the external forcing.

In all HD/MHD simulations featured in the thesis papers an evenly spaced Cartesian grid has been used. In the local models of ISM turbulence featuring the shearing sheet approximation (Hawley et al., 1995; Caunt & Korpi, 2001) there are no special curvatures

within the computational domain, and the constant grid separation, δx, is common to all directions. However, with the Pencil Code, it is also possible to feature non-Cartesian and uneven grid geometries, such as cylindrical geometry.

An FDM solution requires defined boundary conditions, essentially meaning that the boundary values or derivatives must be determined. The simplest and most intuitive conditions are symmetric and periodic. A symmetric boundary condition assumes that the internal structure of a variable is mirrored across the boundary. In the periodic boundary condition, the neighbourhood values outside the boundary take the structure of the field from inside the opposite boundary. In the case of shearing periodic boundaries, a shift in azimuthal direction needs to be taken into account with

$$f(L_x, y, z) = f(0, y + q\Omega_0 L_x t, z). \tag{2.13}$$

where f represents any of the grid variables.

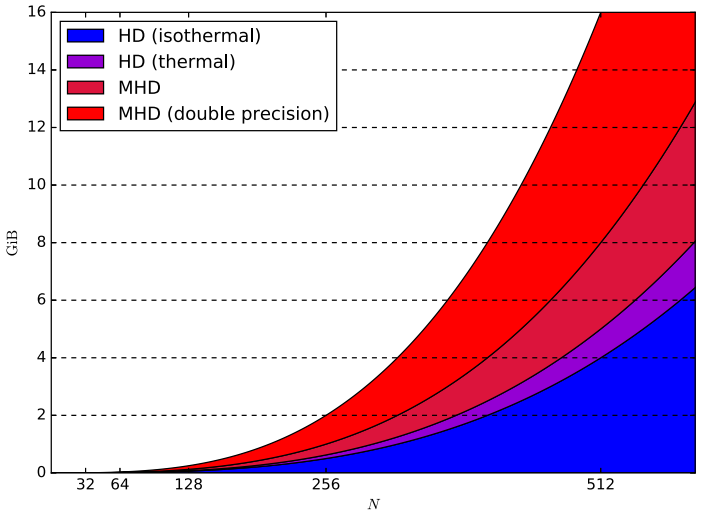

Figure 2.1: Memory usage in GiBs as a function of the resolution (N^3) and number of basic physical variables required (1 for scalars such as density and temperature, 3 for vector quantities such as velocity and magnetic field), taking into account that 2N-Runge-Kutta requires a buffer array equivalent to the size of the main array. While it is possible to fit a high-resolution array into the system memory (e.g. CSC Taito Haswell nodes have 128 GB (119 GiB) memory per node (CSC, 2017)), counting multiple snapshots over long integration times will eventually result in several terabytes of simulation data. Similarly, the number of operation per grid point scales accordingly, but does depend on the number of chosen parameters in the equations and how well the code in question is optimized.

2.3.1 High order schemes are important for turbulence

Turbulence needs time to evolve from an initially laminar state to become fully turbulent. It is not possible to generate a realistic turbulent state as an initial condition, as the turbulence results from many non-linear interactions. Hence, a significant amount of computational time is expended just to attain the onset of a realistic, or "saturated", state where statistical properties of the flow are, in some pertinent sense, steady (see e.g. Gent et al., 2013a,b).

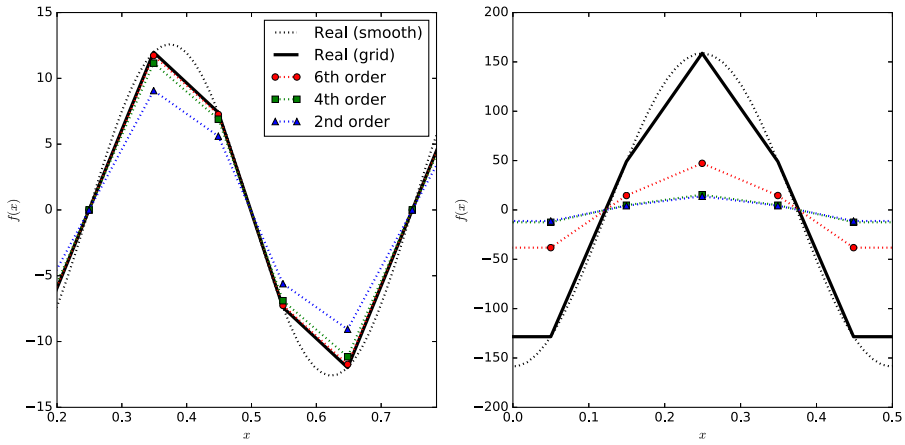

Figure 2.2: Comparison of numerical discretizations of the first and second derivatives of $f(x) = \cos(kx)$, where $k = 0.4\,k_{\mathrm{Ny}}$, with the analytical solutions $f'(x) = -k\sin(kx)$ and $f''(x) = -k^2\cos(kx)$. The different discretizations differ by the order of accuracy.

Because long integration times are needed, the numerical scheme precision becomes an issue. The highest resolvable wavenumber, i.e., the smallest resolvable length scale in relation to the grid resolution, is given by

$$k_{\mathrm{Ny}} = \pi/\delta x. \tag{2.14}$$

In Fig 2.2 simple derivatives of $\cos(kx)$ with wavenumber, $k \lesssim k_{\mathrm{Ny}}$, are presented with derivatives performed using the finite difference operations listed in Table 2.1 (an example of the simple test in Brandenburg, 2003). The increase of the degree of the finite difference operation visibly improves the result. This by itself should motivate the use of high-order schemes for turbulence, although they require more operations. While the low-order operations are less expensive, the loss is precision is undesirable. For example, as integration time increases, the low-order schemes suffer both from strong dissipation and phase errors, leading to badly resolved turbulent waves (Brandenburg, 2003). While high-order schemes are considered to produce stronger Gibbs phenomena (or *wiggles*) which can occur near discontinuities, such as steep velocity gradients in shocks, high-order schemes require less numerical diffusion to dampen such ripples, which can still

make the high-order approach more desirable with all things considered (Brandenburg, 2003).

2.3.2 Quest for numerical stability

It is generally the case that numerical stability is an Achilles heel with simulations of turbulent flows. Astrophysical turbulence contains physical variabilities and instabilities by its very nature and, given that turbulence is the product of very nonlinear effects, this is not a friendly environment for numerical stability in any scheme. Simulation parameters and initial conditions can lead to failure if they fall outside the numerically stable regime, and which sets of parameters will prove favourable cannot easily be anticipated. This is especially true because the scientific applications, for which MHD simulations are typically designated, do not explore safe and familiar parameter spaces. It would, of course, be safe to use excessive diffusivities to stabilize everything. Unless one is performing code tests, however, that is not usually desirable, as the excessive diffusivities would skew the scientific results (Brandenburg, 2003). In addition, one would like to maximize the benefits of a chosen resolution, in which case low as possible diffusivities would be preferred.

The Lax-Richtmyer equivalence theorem states that a consistent finite difference method is convergent if and only if it is stable for a well-posed initial value problem (Lax & Richtmyer, 1956). Generally speaking, a system becomes numerically unstable if the magnitude of errors grows over time, and as FDM relies on recursive operations this is likely if a threshold is exceeded. There are some basic scenarios, which can lead to an MHD simulation crashing. These include *bad values*, wiggles caused by *steep gradients* and *catastrophic turbulent instability*.

When dealing with floating-point arithmetic, the system is susceptible to rounding errors and limits of the defined range. This can be demonstrated with two examples. First, if two big floating-point numbers are subtracted for example `2.123233145e20 - 2.123233135e20` the most of the floating-point digits for the result are not well defined. Second, big and small numbers are not compatible, for example, the sum of floating-point numbers `2.422231179e3 + 5.223245135e20` would not be in the same range for the numbers, leading to loss of information over time. Therefore, the compared numerical values should be of relatable scales and preferable around unity, and in both Pencil Code and Astaroth units can be scaled into dimensionless values to avoid large/small exponents as much as possible. Also, the $\log \rho$ formulation helps with reducing the range of numerical values.

A typical event which can escalate floating-point errors is when a positive definite value turns negative or a result of a calculation produces NaNs. Consider, for example, that due to the erroneous design of the initial condition, an important variable at some grid points, such as density or thermal energy, turns negative or zero. Because FDM requires neighbouring values to resolve the derivative, these invalid values will propagate, eventually killing the simulation with misrepresented floating-point values. This is another reason for both the Pencil Code and Astaroth to express density in logarithmic form $\ln \rho$, permitting negative values and also mitigating against the most extreme gradients

between high and low densities.

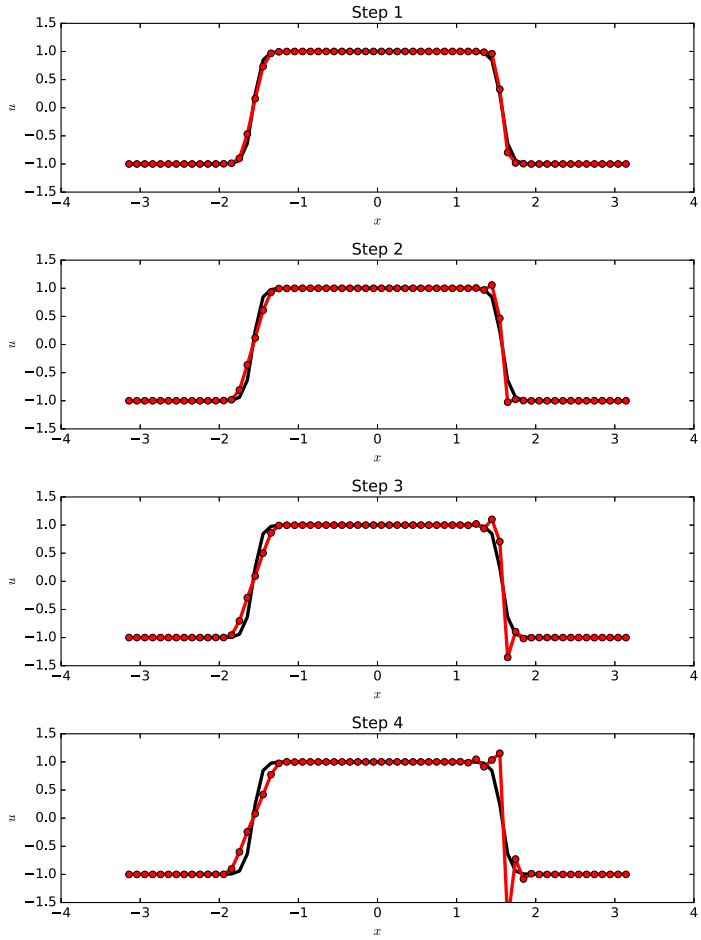

Figure 2.3: Example of a steep gradient with opposing flow directions creating wiggles which grow in time causing numerical instability. Based on an arbitrary 1d FDM solution to Burger's equation $\dot{u} = -uu' + \nu u''$, with initial condition $u = \tanh\left(\frac{\cos x}{\delta x}\right)$ (Idea from Brandenburg, 2003). The wiggles form around the meeting point of opposing flow directions, while the opposite side, lacking such interaction, remains stable.

Most of the time catastrophic numerical values appear due to more specific effects. With FDM, extreme gradients are a common reason for a simulation failure. Astrophysical turbulence can be supersonic and shocks connected to supersonic flows create inconvenient gradients (Caunt & Korpi, 2001). If the gradient of a variable cannot be

properly described within the limits of the resolution, technically approaching the Nyquist frequency limits, then Gibbs phenomenon and aliasing effects can dominate, generating "wiggles" (See example in the Fig. 2.3). If the wiggles produced are weak, they can be still dampened by numerical diffusivities. When the gradient is too strong, the wiggles along with the above-mentioned floating-point errors will propagate, and lead to the uncontrolled localised growth of variable values and then to a crash.

If having obviously ill-posed initial values and the emergence of steep shock gradients were the only reasons for FDM simulations crashing, then setting them up would be fairly simple. Unfortunately, there are also physical effects that can lead to wiggles, erroneous numerical values and numerical instability. As induced turbulence grows in a simulation, it can exceed the bounds of the resolution and stabilizing numerical diffusivities, yielding numerically untenable Reynolds numbers. This growth is not unphysical, but does not fit into machine limitations.

For example, the growth of MRI in the simulations of *Paper IV* reaches a point, at which the system can no longer handle the strength of the velocity gradients. Fortunately, in *Paper IV* this is not a problem, because in that study we are interested in the linear growth phase itself, and with weaker numerical diffusivities more desirable Re and Re_M can be reached.

In unknown parameter spaces, the growth rates and the saturation points of the turbulence are not automatically known. This will mean that most of the new turbulence simulations will likely crash. Therefore, in practice, testing and mapping out suitable parameters for a given simulation will require some experimentation, and can be one of the most work-intensive tasks in a study. Simple models can thus become handy, as in *Paper IV*, because having a reasonable idea about turbulence growth rates and other properties will inform selection of the best parameters for the more computationally expensive simulations.

With the SN-driven turbulence simulations of Gent et al. (2013a,b), which function as the basis for *Paper VI* and *Paper VII*, the system encompasses both nonlinear and supersonic regimes. In such a situation, some special tactics are required to avoid numerical instability in the presence of repeatedly occurring shocks and growing turbulent fluctuations.

2.3.3 Tactics to handle instability

The simplest way to stabilize the system and avoid instability is to set fluid viscosity, thermal diffusivity and magnetic diffusivity coefficients ν, χ $(= K/(\rho c_s))$ and η to sufficiently high levels. The Pencil Code User's Manual (2017) states that for a stable, subsonic simulation, the largest possible values of $\mathrm{Re}_{\mathrm{mesh}}$,

$$\mathrm{Re}_{\mathrm{mesh}} = \frac{\max(|\mathbf{u}|)\,\delta x}{\nu}, \tag{2.15}$$

are around 5.

In addition to having the diffusion coefficients in the MHD equations, the length of the time step has to be adjusted properly. The Courant-Friedrich-Levy (CFL) condition

(Courant et al., 1928) states that for a wave moving across a discretely defined grid, the discrete time step applied to the calculation should be shorter than the wave propagation time across any grid point. In simplified formulation, this would mean for the length of the time-step δt that

$$\delta t < \delta x/u, \quad \delta t < \delta x^2/\nu \tag{2.16}$$

for velocity and diffusion, respectively. Essentially, the time step should be short enough, that the physics effects remain well resolved. Both Pencil Code and Astaroth adjust the time step based on resolution, diffusivities and velocity using the CFL-condition. The CFL-condition has important implications for computational requirements relating to resolution, which will be discussed further in the next section.

While optimally adjusting diffusivities and time step guarantees stability, at least for low-Ma flows, high bulk diffusivities can smooth out details and interesting aspects of the flow (Caunt & Korpi, 2001). Hence, less invasive approaches can be useful. Shock viscosity can be used to detect and resolve steepening shock fronts, only where they occur (Von Neumann & Richtmyer, 1950). In grid locations i where $\nabla \cdot \mathbf{u} < 0$

$$\nu_i^{\text{shock}} = c_{\text{shock}} \delta x_i^2 |\nabla \cdot \mathbf{u}|, \tag{2.17}$$

additonal shock viscosity, ν_i^{shock}, is added locally, with c_{shock} being a constant coefficient. This acts as an artificial, localized, pressure that prevents shock from compressing into sub-grid scales, which would lead to the loss of information and a catastrophic numerical instability.

Another widely used tool is to induce hyperdiffusion, for example, by the upwinding method for derivative operations, such as $\mathbf{u} \cdot \nabla \ln \rho$ and $\mathbf{u} \cdot \nabla s$ (Dobler et al., 2006). With upwinding, the point farthest downstream in the derivative operation is excluded. This will help to stabilize some of the wiggles that propagate in density and entropy, as such a finite difference stencil will afford less freedom to numerical oscillations. In upwinding for the sixth order situation (Dobler et al., 2006, Appendix B) the first derivative

$$D_{\text{cent},6}\Big(f_i\Big) = \frac{-f_{i-3} + 9f_{i-2} - 45f_{i-1} + 45f_{i+1} - 9f_{i+2} + f_{i+3}}{60\delta x} \tag{2.18}$$

is then replaced by

$$D_{\text{upw},5}\Big(f_i\Big) = \frac{-2f_{i-3} + 15f_{i-2} - 60f_{i-1} + 20f_i + 45f_{i+1} - 9f_{i+2}}{60\delta x}. \tag{2.19}$$

The choices of various hyperviscous operations which can to detect and remove wiggles, will depend on the problem at hand.

Naturally, apart from implementing stabilizing viscosity and numerical functionality, there is the option of increasing resolution. In such case, both a larger number of grid points and a shortened time step (due to the CFL-condition) increases the computational requirements. This tends towards the need for parallelization of the problem.

2.3.4 Parallelization and domain decomposition

When performing FDM calculations with multiple cores, the computational domain can be subdivided, with one sub-grid per *process* (e.g. a CPU). This may include one or more cores depending on the approach. This *domain decomposition* requires communication between CPUs, typically done with the *Message Passing Interface* (MPI)[2] (Gropp et al., 1996), which has become a standard tool for majority of computational science.

Decomposing the grid for FDM is straightforward. First, the numerical grid is divided into a suitable number of parts. Second, because 6th-order FDM requires three adjacent points in each coordinate directions to calculate derivatives, each decomposed subdomain requires three boundary points on all boundary surfaces. These *ghost zones* must contain the information from the neighbouring subdomains. If the subdomain contains part of the boundary of the whole domain, the specific boundary condition must be applied there. Therefore, parallelization requires only that the ghost zones are communicated between neighbours, typically with the help of MPI. Otherwise, the only regular collective operations are to obtain diagnostics, such as mean, maxima or minima of specified properties, derived from the variables.

However, because information has to be communicated between the processes, there are limitations with respect to both weak and strong scaling of the computations. *Weak scaling* relates to how a code scales up when the number of processors is increased proportionally to the size of the problem. FDM schemes benefit from straightforward domain decomposition, and often perfect scaling can be reached. If a functional balance is maintained between the number of processes and grid resolution, there is neither a communication bottleneck nor too high a workload per process. This is illustrated in Fig. 2.4 (top). There is an optimal relation between the number of processes P and the resolution N^3. Without ghost zones, the number of grid points per process is

$$W = \frac{N^3}{P}. \tag{2.20}$$

If assuming a Pencil Code default domain split in y and z directions[3], the effective number of grid points per process, with ghost zone size $Q = 6$ (both sides), is

$$W_{\rm eff} = (N + Q) \cdot \left(\frac{N}{\sqrt{P}} + Q \right)^2. \tag{2.21}$$

The Pencil Code User's Manual (2017) states that if $W_{\rm eff}/W = 1.20 - 1.25$, meaning that $20 - 25\%$ of the work is done on the ghost zones, there is a good balance between N and P. This relation is illustrated by the black curve in the Fig. 2.4 (top). With a large enough machine, it is possible to obtain such proportionality.

The real issue with the weak scaling is the time step. A time step following the CFL-criteria has to be shorter when the resolution increases (see Fig. 2.4, bottom). Therefore,

[2] `http://mpi-forum.org/`

[3] Pencil Code can split domains in all coordinate directions, but this domain division is the most convenient to utilize the 1d "pencils" design.

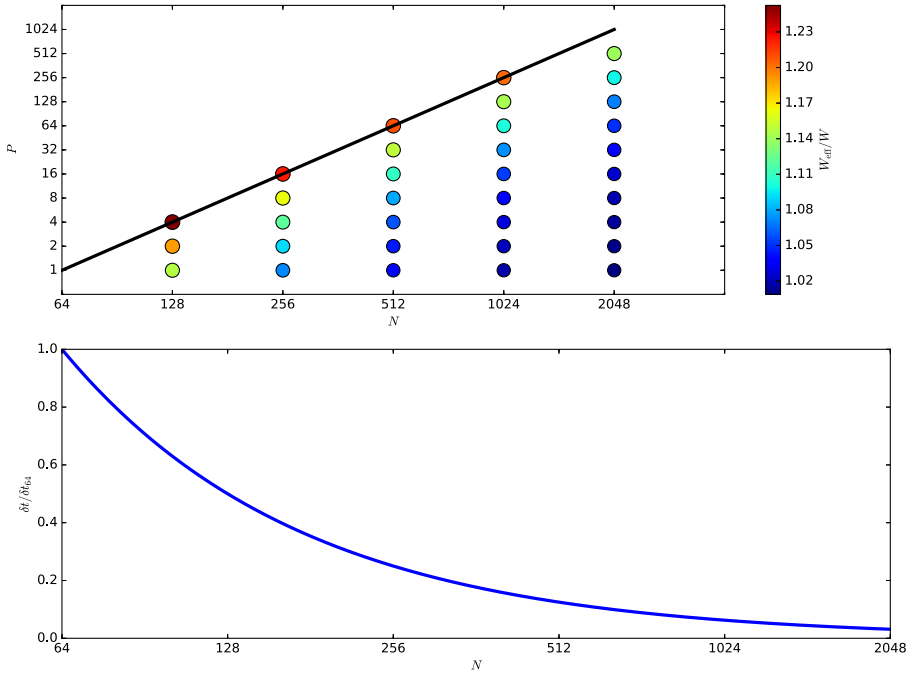

Figure 2.4: (*Top*) Number of utilized grid points in relation to a grid without ghost zones W_{eff}/W (Eq. 2.21, shown by the colour bar), as a function of both the total process count P and the cubic grid resolution N^3. The black line traces $W_{\mathrm{eff}}/W = 1.20 - 1.25$ points. (*Bottom*) Relative change in time step length as a function of increasing grid resolution. δt_{64} denotes the length of a single time step time with $N = 64$, both steps are calculated with CFL condition (Eq. 2.16)

.

while it is possible to resolve finer details in turbulence, to reach a specific time in the growth of the turbulence, requires more computational steps, and therefore more time to reach a saturated state of turbulence. Therefore, if the principle of maintaining scaling in the weak sense is followed, a better spatial resolution can be gained, but speed up in terms of time development is not guaranteed.

To speed up computations, increasing the number of CPUs without changing the resolution is required for what is called *strong scaling*. In this case, the limitations of FDM become more pronounced, as the time required for communication becomes an issue. Fig. 2.5 presents a schematic description of this, where increasing the number of processes means the increasing communication lag impacts negatively on the total wall clock required to compute one time step (δT). The issues with both weak and strong scaling will mean that, in the long run, merely increasing the number of MPI processes

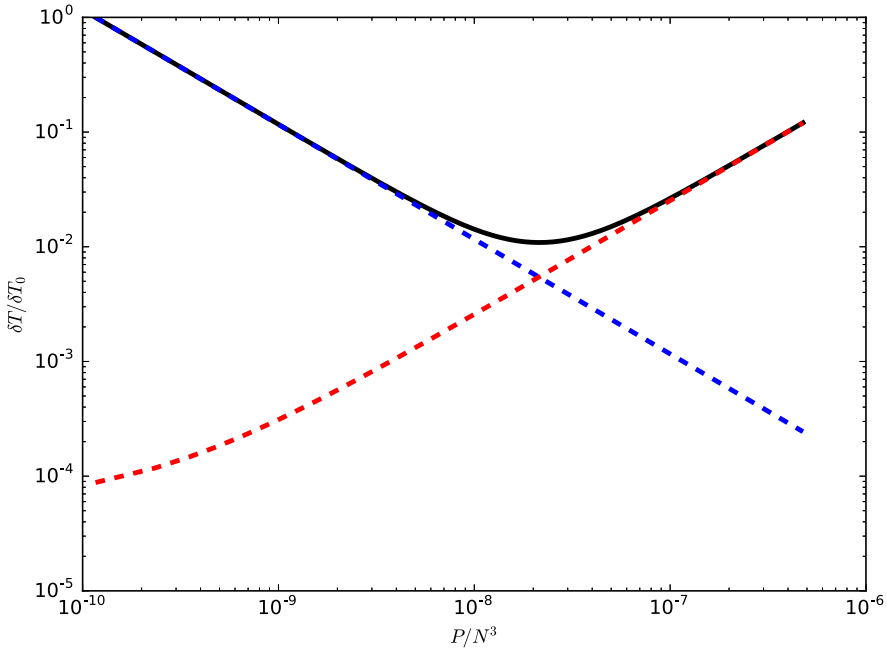

Figure 2.5: A schematic demonstration of strong scaling. The change in the wall clock time for computing a step (δT) relative to the wall clock time taken by a single CPU (δT_0). The black, blue and red lines correspond to total computing time, time spent on the main grid and time spent on communication/ghost zones respectively. With a too high number of processes the communication lag can cancel out the gained benefit.

cannot be an efficient way to improve performance.

2.4 High order finite differences with GPUs

One of the more potent tools among the current technology are systems, which can utilize multiple processor cores more efficiently than a traditional processor, such as Intel Xeon Phi type multiprocessors and GPUs. Within the scope of this thesis, a GPU implementation has been developed. Being primarily developed for enhancing computer gaming graphics performance, GPUs have been built to handle simple floating-point operations quickly and repeatedly. With improving GPU-technologies, application programming interfaces (API) have also been developed for making the use of GPUs easier and

more versatile. These include *NVIDIA CUDA*[4], *OpenCL*[5], and *OpenACC*[6], which enable general-purpose computing on graphics processing units (GPGPU) for ordinary scientists.

However, GPGPU is still a fairly unexplored frontier, and there are risks involved. In particular, although API tools are gradually improving, programming efficient GPU code can require a lot of work, especially when attending memory management and usage in detail (e.g., different types of GPU memory have different read-write latencies). Therefore, while *Paper V* discusses the actual methods and algorithms we developed, the aim of this chapter is to give more context to the results, offer some advice to a reader interested in GPU development and provide some further ideas as to how the GPGPU approach could be usefully utilized with MHD turbulence computations.

2.4.1 Astaroth code

Astaroth is a proof-of-concept code which utilizes GPUs for computing 6th order finite difference method with 3rd order 2N-Runge-Kutta method (Stanescu & Habashi, 1998; Brandenburg, 2003). As such, it utilizes the central building blocks of the Pencil Code to examine whether a high-order solver, in the first place, can benefit from GPUs, as the communication overhead is great. A simplified approach is achieved by keeping physics on the level of isothermal hydrodynamics and focusing on optimizing the code for a single GPU.

However, Astaroth has been created in a way that it can perform scientifically useful tasks on its own and is modularly expandable. It would have been simpler to build a code for mere algorithm testing, but that way essential practicalities for code development could have been disregarded by doing regrettable shortcuts, like not taking into account the realities how such tools are used by the domain scientists, and how proper physical functioning of the code can be verified when new features are included. Therefore, Astaroth contains tools for initializing independent computational setups and a set of scripts to analyze the produced data. It can also output various collective diagnostics and animation snapshots.

Astaroth has been built using NVIDIA CUDA toolkit [7] and with connected C/C++ programming language. In addition, it contains tools made with Python[8] programming language for the purposes of data analysis and visualization. While the GPU methods presented bellow apply to Astaroth, most of the core principles of CUDA apply for GPGPU computing in general.

The development of the Astaroth code has been a long process, having started already in 2012. Astaroth code is named after a demon mentioned in various texts of mysticism and demonology (e.g. Weyer, 1568; de Plancy, 1863). It is an apt name for the code, as the demon Astaroth is connected with science, mathematics and laziness. He is a great, strong duke, who commands many legions; and similarly, Astaroth commands

[4] `https://developer.nvidia.com/about-cuda`
[5] `https://www.khronos.org/opencl/`
[6] `https://www.openacc.org/`
[7] `https://developer.nvidia.com/cuda-toolkit`
[8] `https://www.python.org/`

legions of CUDA threads to compute turbulent flows – with or without the sulphurous fires of Hell.

2.4.2 CUDA programming model

GPUs function as an array of streaming multiprocessors (NVIDIA, 2017). This makes it possible for them to perform several floating-point operations simultaneously. However, when programming a GPU code, some attention to the programming model is required for it to perform well and produce correct results. First, programs are executed inside GPUs along parallel threads, and therefore kernels are programmed from the perspective of a single thread. Second, GPUs are "stupid", and so attention should be paid to how the memory layouts and communication are designed.

When creating a GPU program, the system has to be divided into two primary parts, a *host* and a *device*. The host side is the conventional CPU system where the usual programming conventions apply. The device denotes the GPU itself. Both of these function as a separate unit, which do not communicate unless explicitly stated. In a simple GPU program, the system is initialized at the host side, the relevant arrays and variables are communicated to the device side, where the heavy computation is performed, and the results are transferred back to the host side for further processing. Communication is slow between the host and device, however, and should be kept at the minimum.

GPU instructions are called from a subroutine-type called kernel, which can be invoked from the host side. A GPU system employs a Single-Instruction, Multiple-Thread (SIMT) architecture (NVIDIA, 2017). Therefore, a kernel is programmed and executed from the perspective of a single thread following instruction-level parallelism. A CUDA GPU computes threads in batches of 32 called *warps*. A set of threads can be explicitly grouped into *blocks* which share some memory with other threads. Although a rough GPU program can be written with just grouping the given problem into threads and blocks, to achieve maximum efficiency and occupancy requires special considerations for memory. The essential types of CUDA memory are *global*, *shared*, *local* and *constant memory*. There is also *texture* memory, but that is outside of the functionality of the Astaroth code, and therefore not discussed.

The bulk of the data can be kept in the *global memory*. Global memory is accessible to all threads and has the most space in megabytes. The drawback of the global memory is its slowness. It is recommended that global memory is prioritized for large-scale storage of the data, and other memory types should be used when quick, repeated accesses are needed.

The size of the global memory limits the maximum grid size to be computed on a single GPU. As this amounts to less, even with dedicated NVIDIA Tesla cards than on a general HPC node, communication between multiple GPUs is needed, which brings about new latency issues. The current stable version of Astaroth is only focused on a single GPU, which is one of its present limitations. Regardless, a NVIDIA Tesla card contains in between 5 to 15 GB of memory[9], meaning that a sizeable computational grid can be

[9] `http://www.nvidia.com/content/tesla/pdf/nvidia-tesla-kepler-family-datasheet.pdf`

used. Compared to Fig. 2.1, it would be possible to fit even a single precision full MHD grid with 512^3 points to the global memory of some current Tesla devices, allowing for many possibilities.

The *shared memory* can be accessed by a whole thread block. It is fast, but also of limited size (48 KB), and therefore has to be used intelligently. Both the 19-point and 55-point methods presented in the *Paper V* try to handle this limit with a cache blocking method and some of the aspect of shared memory usage will be addressed in the next section.

The *local memory* can only be seen by a single thread. If the kernel specific variables can be kept within the bounds of the maximum number of registers (64K/32K per thread block), the memory access is fast. However, if register spilling happens, local memory can be almost as slow as the global memory to access.

The *constant memory* is useful for storing global variables, such as various coefficients (e.g. an isothermal c_s, a constant ν). The constant memory cannot be written into from the GPU side, but it provides fast and available memory regardless of thread/block index. That said, a programmer should take care to define a constant explicitly, as floating point numbers written in a kernel source code will be interpreted as local memory, not as constants.

2.4.3 Finite difference method with GPUs

High-order FDM, due to its large stencil size, requires special considerations and techniques with its implementation onto a GPU. Proper optimization needs proper memory utilization to achieve full occupancy. Otherwise, the gained speedup can be lost due to the relative slowness of memory accesses.

As large as possible part of the grid should be read into the shared memory, corresponding to the utilized amount of threads in a block. In this case, the challenge posed by the high-order finite differences is that every separate block of shared memory requires a ghost zone like halo, and that the number of points in the halo can be high compared to the actual computed grid points. In *Paper V*, 55-point and 19-point methods used shared memory grids shaped

$$(\tau_x + 2R) \times (\tau_y + 2R) \times (\tau_z + 2R), \tag{2.22}$$

$$(\tau_x + 2R) \times (\tau_y + 2R) \tag{2.23}$$

respectively, where $R = 3$ is the length of the stencil, and τ_i denote the dimensions of the thread block. For example, with the 55-point method $\tau_x = \tau_y = \tau_z = 8$, meaning that the ratio between the number of effective grid points and halo points, $\tau_{\mathrm{tot}}/R_{\mathrm{tot}} = 0.23$, is dominated by the halo.

To decrease the number of read-writes from the global device memory, the limit of the shared memory space can be compensated with cache blocking. In this way, a thread block is allocated with a larger area of the main grid than its size, and its location is moved gradually, updating parts of the halo points each step.

Despite this, the very limited shared memory size is a clear bottleneck for high order stencil computation, because the required amount of memory is large in relation to the number of threads. Especially with more variables/grids added, the impact of read-write latencies will increase. On the other hand, if the number of variables is kept the same but more mathematical operations are added per grid point, then the cost of computation is cheap. Therefore, this suggests that memory should be used sparingly, while the amount of computed operations should be maximized.

Paper V also shows that the reading order of the shared memory can have a big effect on performance. The gradient of divergence in the viscosity term of the Navier-Stokes equation, $\nu\frac{1}{3}\nabla(\nabla\cdot\mathbf{u})$, is challenging to compute, as it requires cross derivatives (i.e. $\frac{\partial}{\partial y}\frac{\partial f}{\partial x}$). The performance advantage of the 19-point method is achieved, because there explicit gross derivatives are not required, by utilizing two separate passes when calculating the derivatives, and therefore the memory access patterns become more beneficial.

It would have naturally been possible to adapt the method in Astaroth for simpler viscosity terms. This would certainly have made optimization easier, but the cost would have been to postpone the full problem until a later time, and therefore not recognizing some essential challenges early on. The modifications needed to include a new method of feature could have become very problematic to implement later on due to the intricacies of GPU programming, which should be accounted for when building a good foundation to the code.

2.4.4 Practical uses for GPU approach

It will take a long time for GPU tools, such as Astaroth to develop to the level of the well-established multiphysics MHD solvers such as the Pencil Code. The future course for Astaroth is potentially integration with the larger framework of the Pencil Code, as its physical capacities continue to evolve beyond the presented work here. In a shorter time frame, it is legitimate to ask how useful the more limited GPU solvers are for practical applications in the near future. However, there is a straightforward application. This is to explore parameter spaces for physical models.

Considering that turbulence is a nonlinear phenomenon and requires time to develop in the simulation setup, it is not immediately obvious which parameters and initial conditions are significant. Therefore, a GPU-accelerated solver can be used prior to the launch of heavier production runs for coarse mapping of the parameter space to guide the modelling efforts, in a similar way as was done for MRI in the *Paper IV*.

In addition, GPU solvers could be used as a fast testbed for novel setups and regimes. Potentially, the tests could be run even on a local workstation with a dedicated GPU device, instead of queuing and spending processor time on a cluster.

3 Observing the interstellar medium

As the ISM consists of materials with different radiative properties, it can be observed through various frequency bands. For example, optical Hα emission is characteristic to ionized emission nebulae (e.g. Gaustad et al., 2001), whereas the absorption of light by dust in dense clouds is usually measured using observations at optical and infrared wavelengths (e.g. Mäkelä & Haikala, 2013). Thermal emission of dust and the most of important spectral lines of cold ISM gas are observed at far-infrared and radio wavelengths (e.g. Planck Collaboration XI, 2014; Bergin & Tafalla, 2007). The choice of frequencies depends on the physical question and available instrumentation.

In this thesis, the spectral line emission from cold molecular clouds and far-infrared/sub-millimetre continuum of the interstellar dust grains have a special focus. Molecular lines have been used to look into the cold cloud cores (see e.g. Chapter 5, *Paper II* and *Paper III*), some archived far-infrared observations by the *Spitzer Space Telescope* and *Herschel Space Observatory* has been used in *Paper III* and polarized sub-millimetre continuum thermal emission observed by the *Planck* satellite functions as a central point of comparison for *Paper VI*.

3.1 Molecular line emission

Spectral lines of many molecules can be observed with radio telescopes with heterodyne receivers, and such data can reveal the physical properties of the emitting gas. In particular, the molecular lines can be used to trace the structure of the cold molecular clouds. In dense molecular clouds, most of the mass consists of molecular hydrogen (H_2) . For H_2 the main emission mechanism are,

- *UV-fluorescence*: Absorption of UV photons in the Lyman ($\lambda < 1108$ Å) and Werner bands ($\lambda < 1008$ Å) raise H_2 to excited electronic levels. The decay leads either to dissociation or the molecule is bound to rotational-vibrational levels (Heyer & Dame, 2015).

- *Near-infrared*: Rotational-vibrational lines are excited by collisions in hot post-shock gas (several 1000 K) in protostellar flows (Davis & Eisloeffel, 1995).

- *Mid-infrared*: Pure rotational lines excited by collisions with warm gas (> 100 K) (Parmar et al., 1991).

Therefore, probing the bulk of the H_2 in the cold ISM requires observational surrogates to trace the behaviour of the molecular gas.

Carbon monoxide, CO, and ammonia, NH_3, are examples of commonly observed molecules because they are abundant and easily excited by collisions with H_2 (Ho & Townes, 1983). Molecular spectral lines are intrinsically narrow, which makes it simple to measure radial velocities by the use of the Doppler effect. This way spectral lines can be used to estimate the kinematics of astrophysical objects, as exemplified by *Paper III*. In addition, the spectral line shapes and widths can inform of the presence of shocks (Bachiller et al., 1991) and radial velocity dispersion (Tobin et al., 2011) respectively.

Apart from the Zeeman effect and weak linear polarization that are observable in certain circumstances (Hansen, 1982; Goldreich & Kylafis, 1981, 1982; Lunttila et al., 2009), molecular lines in general are not sensitive to the magnetic field. In addition, synchrotron emission and Faraday rotation observations with radio telescope are used to estimate magnetic fields in galaxies (Beck, 2016), but such methods are also beyond the scope of this thesis. However, often the observed kinematics from molecular lines are related to the presence of magnetic fields. For example, it is well known that the magnetic field plays an important role in the cloud collapse leading to star formation and is essential in generating protostellar outflows (e.g. Matsumoto et al., 2017). This matter is explored further in Chapter 5.

When observations of multiple molecular spectral lines are combined with astrochemical modelling (see e.g. van Dishoeck & Blake, 1998; Sipilä, 2013, and references therein), conclusions can be made of the physical state of the environment. Indeed, the proper interpretation of spectral lines has to be based on understanding in which physical context a particular molecule can exist. For example, nitrogen compounds do well in cold molecular clouds (van Dishoeck & Blake, 1998), while H_2O can form within protostellar outflows (Suutarinen et al., 2014). Molecules can also freeze on the dust grains and thus the lack of molecular emission might not signify the lack of molecule itself.

3.1.1 NH_3 (J,K) line emission

The symmetric top molecule NH_3 can serve as an example of the use of molecular spectral line emission as a probe of the physical conditions in interstellar clouds, as it was the primary focus on *Paper II* and *Paper III*. There, primarily NH_3 (J=1,K=1) inversion line emission observations were used to explore internal properties of the Cha-MMS1 core.

The standard astronomical interpretation of the rotation-inversion spectra of NH_3 is described by Ho & Townes (1983). Apart from CO, ammonia is among the most important tracer molecules, abundant in the cold interstellar medium. The relatively high abundance of NH_3 allows it to be used with a wide variety of molecular clouds, and because it has multiple structural transitional states sensitive to a wide range of excitation conditions, it can provide information on the physical state of the source of the emission.

The spectral lines of NH_3 are distributed/split into multiple hyperfine components. In particular, the (J=1,K=1) inversion transition is split into 18 individual components (Ho & Townes, 1983). These are distributed into five well-resolved groups, separated by

$\sim$ 1 MHz. The main group contains (exactly) 50% of the emission. This behaviour is well demonstrated in the NH_3 (1,1) spectra shown in *Paper III*. A benefit of this line structure is that, different components having varying optical depths, the self-absorption causes less loss of information than it would with emission producing a smaller number of discernible spikes. In *Paper III*, where self-absorption is high, the radial velocities of the molecular gas can be effectively inferred, because the self-absorption effects only the main group of hyperfine components.

Another benefit of ammonia is that, compared to many other abundant molecules, NH_3 freezes slowly onto dust grains, therefore it can be well used in probing the very cold, dense molecular clouds cores often connected with star formation. Indeed Tafalla et al. (2006) have stated that mainly nitrogen compounds, such as NH_3 and N_2H^+, are present in a gas phase within the cold cores, emphasizing why NH_3 has such an important role in this thesis.

3.2 Dust and polarization

Dust is heated by the surrounding stellar radiation, and the dust, although cold, produces thermal emission (Steinacker et al., 2013). In the presence of a magnetic field, non-spherical spinning dust particles tend to align their spin-axes (statistically) with the magnetic field lines (that is, the preferred direction of their long-axes is perpendicular to the magnetic field, Andersson et al., 2015). Light waves with electric vectors oriented parallel with the long-axes of grains experience greater extinction than light with electric vectors perpendicular to the long axes. This results in the partial interstellar linear polarization of starlight where radiation is strongest in the magnetic field direction. In contrast, thermal emission from dust grains at far-infrared and submillimetre wavelengths is strongest in a direction which is perpendicular to magnetic field lines.

The local emissivity of the dust can be expressed as modified black body emission

$$j_{\mathrm{d},\nu} = \kappa_{\mathrm{abs},\nu} \rho_{\mathrm{d}} B_\nu(T), \tag{3.1}$$

where $B_\nu(T)$ is the Planck function, ρ_{d} the local dust density and $\kappa_{\mathrm{abs},\nu}$ absorption coefficient of dust at the frequency ν. This applies fairly well to the large grains, but for small grains, such as PAHs, will require more nuanced assumptions (Steinacker et al., 2013).

Because an approximate dust-to-gas ratio can be assumed (Zubko et al., 2004), the emission and absorption of the interstellar dust are valuable phenomena when exploring the structure of the ISM. It is relatively easy to map dust emission over extended sky regions with satellites like *IRAS*, *Akari*, *Planck* and *Herschel Space Observatory*. Particularly Planck has performed an extensive mapping of dust polarization over the whole sky, an giving indication of large-scale magnetic fields (Planck Collaboration Int. XIX, 2015).

The two main theories for interstellar dust grain alignment with the magnetic field are called *paramagnetic relaxation*, and *radiative alignment* (Andersson et al., 2015). The basic principle of paramagnetic alignment, as suggested originally by Davis & Greenstein

(1951), is that the dissipation of angular momentum components perpendicular to the magnetic field makes the grain to align with the magnetic field. This, however, requires that relaxation times of the dissipation is shorter than the randomization time connected to the gaseous collisions. Paramagnetic alignment appears to be inefficient for large grains ($a > 0.1$ μm), although it might remain functional mechanism for small grains ($a \sim 0.01$ μm) (Andersson et al., 2015).

Radiative alignment is currently the most accepted theory for dust alignment (Andersson et al., 2015). It was originally formulated by Dolginov & Mytrophanov (1976), and later substantiated with numerical calculations by Draine & Weingartner (1996). With radiative alignment, the dust particles align their rotational long axes with the magnetic field direction with a combination of paramagnetic interaction and radiative torque. More specifically, radiative torque helps to overcome the randomization caused by the thermal dust collisions (Pelkonen et al., 2009). The rotating grain with a fast precession finds the stationary point where its rotational axis and magnetic field are parallel to each other (Andersson et al., 2015).

Regardless of the exact mechanism behind dust grain alignments, the linear polarization Stokes components I, Q, U can be examined (Fiege & Pudritz, 2000; Pelkonen et al., 2009; Planck Collaboration Int. XX, 2015), as has been done in the *Paper VI*. In that case, the influence of the magnetic field is a macroscopic effect where microscopic alignment behaviours is approximated with a coefficient. However, as *Paper VI* deals with emission from very large scales, issues like radiative shielding of the dust grains (Pelkonen et al., 2009) will not have a substantial effect.

3.3 Radio and submillimetre observations

To study the types of emission described above, radio and submillimetre observations are required. In general, when observing long wavelengths, the resolution is relatively low when compared to optical telescopes. This can be compensated with the aid of interferometry, but with added disadvantages like insensitivity to large-scale emission. Therefore, when analyzing and interpreting observational data some key aspects have to be kept in mind. When using single-dish radio telescopes observations are possible with both heterodyne receivers and bolometers.

A heterodyne receiver (e.g. Baryshev et al., 2015) makes it possible to measure very high-resolution spectra for detailed studies of molecular lines. A Heterodyne receiver perceives emission as a function of frequency from an area of the sky which depends on the telescope beam size (which is proportional to $\sim \lambda/D$; D being the diameter of the dish). Building a spectral line map using a single dish telescope requires multiple pointings, and can be very time consuming depending on the required sensitivity and the total area to be mapped. The receiver works by converting the signal to a lower frequency. This lowers the added noise and facilitates amplification. The receiver also preserves the phase of incoming radiation, which enables very high spectral resolution and correlation of signals from different antennas, which is useful in interferometry.

Measuring the submillimetre thermal emission from the cold dust is more tricky. Such

observations can be made with bolometer array type receivers (such as Submillimetre Common-User Bolometer Array, or SCUBA, on the James Clerk Maxwell Telescope, Holland et al., 2013). In bolometer array type receivers, impacting photons change temperatures in the respective receiving elements, which are then measured via observed changes in the electrical resistances of the said elements. Ground-based bolometer observations are affected by fluctuations in the sky brightness, which means that they are only sensitive to relatively bright and compact targets. In ground-based mappings, extended emission which is larger than the footprint of the bolometer array is not recovered because the elimination of the fluctuating atmospheric signal leads to signal loss. Fortunately, space-based observations, most recent being from *Planck* and *Herschel Space Observatory*, avoid this problem by carrying out observations outside the atmosphere. This has made it possible to make extended observations on far-infrared and submillimetre frequencies, such a Planck HFI measurements of polarized dust emission (Planck Collaboration XI, 2014; Planck Collaboration Int. XIX, 2015).

3.3.1 Interferometry

Interferometry is a technique of obtaining improved resolution by combining observations from multiple telescopes. Due to the long wavelengths, interferometry is technically most simple to implement at radio frequencies.

With interferometry, several coordinated telescopes are pointed towards a particular point in the sky (see e.g. ALMA Partnership et al., 2016, for many practical aspects of radio interferometry). An interferometer measures the interference pattern produced by a pair of antennas. The interference pattern is related to the sky brightness by the Fourier transform: the measured quantity, the complex visibility $V(u, v)$, is the 2D Fourier transform of the surface brightness distribution $I(x, y)$. Using antenna pairs with different separations, samples are taken of the complex visibility at points (u_i, v_i). The image fidelity depends on how many samples are taken. The image fidelity can be improved by increasing the number of antennas, and by tracking the source as Earth rotates, which increases the number of different baselines measured, and thereby improves the image quality. The resulting image can be a 3-dimensional data cube with two sky coordinate dimensions and one frequency dimension. However, the with a single pointing the angular extent of the recovered image cannot exceed the size of the primary beam width of the telescopes $\sim \lambda/D$, where D is the diameter of the antennae aperture.

The drawback of interferometry is that large-scale emission is lost. Emission features larger than $\sim 0.6\lambda/b_{\min}$, where $b_{\min}$ is the diameter of the shortest baseline (distance between antennae pair), cannot be recovered. The loss of emission increases when receiving interferometer elements are spread further apart. Therefore, a practical balance between resolution and large-scale emission has to be found. Also for this reason, single dish observations remain useful.

In the best case, it is good to combine single dish/compact array observation with the high-resolution interferometry. For example in Atacama Large Millimeter Array (ALMA) telescope complex, Atacama Compact Array (ACA) can be used in combination the larger

main array. ACA helps to extend the measurement to cover larger scales, but to recover all emission on scales ($\sim \lambda/D$) requires also Total Power (TP) antennas, that is, single-dish measurement of the same field (with a similar antenna as used for the interferometry). And if such combination is not possible, one could do like in *Paper III*, where we compare both Australian Telescope Compact Array (ATCA) interferometry and Parkes Telescope single dish observations to gain a better understanding of the situation.

4 Magnetic turbulence in the interstellar medium

Turbulent behaviour of the ISM is driven by multiple processes, which are distributed across multiple scales. In addition, the galactic ISM is subject to rotation and its non-uniformities, that cause the excitation of large-scale magnetic fields, all adding anisotropies to the flow. Therefore, understanding interstellar turbulence is a challenging task beyond the reach of laboratory experiments or analytical treatment. The physical conditions in the ISM are extreme, varying from extremely cold in the molecular clouds to extremely hot in the vicinity of SNRs, all thermodynamic quantities varying by several orders of magnitude (see Table 1.1).

Galaxies are disk systems that can be observed to rotate differentially. The deduction of the rotation laws are simple only for external galaxies, while pose a challenging task for the Milky Way, inside of which us observers live. In differentially rotating disks, the magnetic field plays a special role. Such disks are hydrodynamically stable in the case of Keplerian, applicable to accretion disks, and flat rotation curves, applicable to galactic disks, but are de-stabilised in the presence of weak magnetic fields (Chandrasekhar, 1960; Balbus & Hawley, 1998). The presence of magnetic fields, therefore, makes the disks turbulent, and thereby enables enhanced turbulent diffusion, and for example efficient accretion in accretion disks.

The effect of ISM turbulence is pervasive. SNe, the most powerful source of interstellar turbulence, in focus in *Paper VI* and *Paper VII*, produce effects that cascade towards smaller scales which affect molecular clouds and star formation. The process then feeds back to the larger scales by the birth of new stars generating new SNe (Padoan et al., 2017). The connection between large and small scales is one of the leading themes of this thesis, and is discussed in this chapter.

4.1 Differential rotation

One shared key feature of a disk system is its differential rotation. For a differentially rotating disk, the angular velocity changes as a function of distance from the disks centre as

$$\Omega \propto r^{-q}, \tag{4.1}$$

where the shear parameter q describes the shape of the profile. For a Keplerian disk, such as accretion disks around young stars, $q = 3/2$, while galaxies rotate with a flat rotation curve, $q = 1$.

In the local approximation used in our numerical models, namely the shearing sheet approximation, the shear in the angular velocity translates to a linear shearing velocity, if $L_x, L_y, L_z \ll R$, giving an azimuthal component to the system velocity,

$$u_{y,0} = -q\Omega x\hat{\mathbf{y}}. \tag{4.2}$$

Using this approximation, it is possible to include the effect of the large-scale shear into a local model by simply modifying the boundary conditions to account for the linear shift caused by the shear, and including the advection by this basic flow to the equations (Hawley et al., 1995).

The presence of shear induced anistoropies to the flow generates turbulent stresses, and can also de-stabilise the flow if a magnetic field is present through the magnetorotational instability (MRI) discussed later in this chapter. However, in addition to their different rotation profiles, both galactic and protostellar disks are also influenced by the other processes. In galactic disks, the system is heavily affected by stellar energy input (Korpi, 1999). The stars heat and ionize the surrounding ISM, produce stellar winds, and their evolution leads to other energetic events such as SNe. In that situation, as we argue in *Paper I*, MRI is damped by the efficient turbulent mixing caused by the SNe, at least in galaxies with star formation rates comparable to the Milky Way.

In protostellar disks, the inflow from the collapsing prestellar core and outflow resulting from the twisted magnetic field have great dynamical significance, particularly at the early stages when the disk is young (Matsumoto et al., 2017). Also, in the later stages of star formation, heating by the central protostar will substantially influence the disk (McKee & Ostriker, 2007). However, the possible presence of MRI will depend of the stage and location of the disk as the conditions of ionization and the connected ohmic diffusivities will vary (Jin, 1996; Balbus, 2003).

In this chapter, the focus is on the galactic disks, while Chapter 5 discusses the early stages of star formation.

4.2 Possible sources of turbulence

There are many potential sources of ISM turbulence, and in the most realistic case many sources exits simultaneously, unless they are damped by some other process. Here we focus on two known mechanisms, MRI and SN-driven turbulence. There are naturally other mechanisms, such as Parker instability (e.g. Shibata, K. and Matsumoto, R., 1991; Parker, 1992; Hanasz et al., 2002), thermal instability (e.g. Brandenburg et al., 2007; Mantere & Cole, 2012), and gravitationally-driven instabilities (e.g. Bournaud et al., 2010; Elmegreen, 2011). Of these mechanisms, MRI, SN-forcing, and thermal instability, can be present in the numerical setups studied in this thesis, while Parker and gravitationally driven instabilities cannot be present in our models. Also, as will be discussed later, SNe

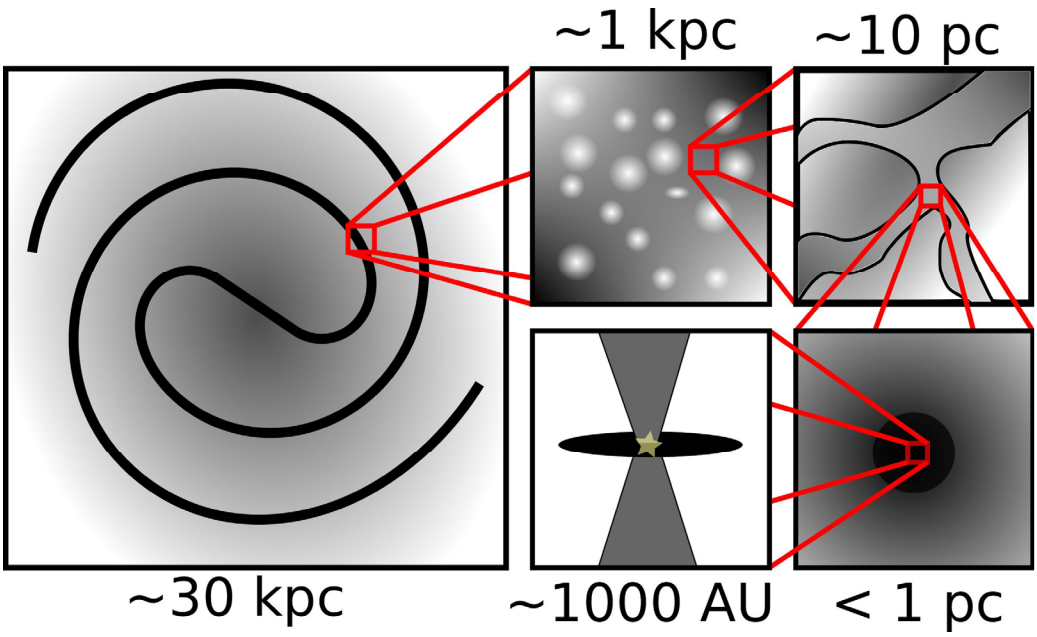

Figure 4.1: Various scales of ISM down to star formation. In order, the scales correspond to the Milky Way scale, SN-driven turbulence, molecular clouds, dense cold cores and accretion disks around protostars.

are likely dominating the energy input into turbulence. Therefore, in the following, we concentrate on SN-forcing and those instabilities that can occur in our simulations.

From the perspective of the galactic dynamo, created turbulence affects both growth and dissipation of the magnetic field. On one hand, helical turbulence is believed to contribute to amplifying the magnetic field and lead to the formation of large-scale fields through the turbulent dynamo process, while on the other, strong stirring will enhance the diffusion greatly from the molecular values, leading to decay of the magnetic field but also, as claimed in *Paper I* and verified in *Paper IV*, to the damping of the MRI. MRI is also known to produce a dynamo effect as an inevitable consequence in the non-linear stage of the instability (Brandenburg et al., 1995), and as such its existence or non-existence is meaningful when examining the galactic dynamo as a whole.

4.2.1 Magnetorotational instability

The principle of MRI was originally introduced by Velikhov (1959) and Chandrasekhar (1960, 1961), but the work of Balbus & Hawley (1991) and Hawley & Balbus (1991) gave it astrophysical relevance. MRI is an instability that can occur in a weakly magnetized disk system which is rotating differentially. While this initial weak field is not strong

enough to influence the disk on large scales, dominated by the rotational energy of the disk, it forms a sufficient seed field for the growth of the instability.

Consider two small fluid elements which are connected by a weak magnetic field, which rotate with different angular velocity, inner element rotating more rapidly (Balbus & Hawley, 1998). As the fluid elements move apart, the magnetic tension between them increases. As the magnetic tension seeks balance, the inner fluid element loses angular momentum to the outer element, which causes the inner element to drop into lower orbit and the outer element to expand outwards. This process is repeated and finally it runs off and turbulence is created.

In an MRI active system, the turbulent stresses, namely the Reynolds stresses, $\langle u_i u_j \rangle$, and the Maxwell stresses, $\langle b_i b_j \rangle$, play an important role. In particular, the horizontal stresses extract energy from the shear flow and transfer it to the kinetic and magnetic energy reservoirs, respectively. The Lorentz force connects these two energy reservoirs, and in the non-linear stage, both a self-sustained turbulent flow, but also a dynamo process, is generated and maintained. The special property of the system is that the energy transferred into magnetic form is much more efficient than the tapping of the energy into kinetic form. Therefore, very strong azimuthal magnetic fields are generated as a consequence of the action of the shear to generate the Maxwell stresses. Some other ingredient in the dynamo process, however, is needed to complete the dynamo loop, that is to generate the radial magnetic field. It has been proposed that this effect would have similarities to the alpha-effect arising from helical turbulence (e.g. Brandenburg et al., 1995), but this mechanism is still debated. The end result of an MRI dynamo normally is a superequipartition magnetic field; meaning that the magnetic energy is much larger than the energy contained in the turbulent motions.

The crucial role of turbulent stresses in protostellar disks is their contribution to the angular momentum transport. Already Shakura & Sunyaev (1973) considered that the mass accretion from a disk towards the central object was driven by turbulent viscosity within a magnetic disk. The angular momentum transport outwards, enabled by the turbulent stresses, leads to the accretion of mass inwards in the disk system. The angular momentum flux in a MRI-powered system indeed is orders of magnitude larger than that caused by ordinary molecular viscosity (e.g. Balbus, 2003), and therefore MRI is considered potentially important mechanism for mass accretion in disks, such as around a protostars (McKee & Ostriker, 2007). The MRI angular momentum transfer can also co-exist with spiral density waves which occur on larger scales within the disk (e.g. Heinemann & Papaloizou, 2009; Ju et al., 2017). However, the models featured in this thesis have too small horizontal extent to take such large-scale effects into account.

While the presence of MRI is rather an expected mechanism in accretion disks around young stars, this is not necessarily the case in disk systems where other powerful sources of turbulence are present, providing by themselves a significantly enhanced turbulent diffusion. This question is explored in *Paper I*, *Paper IV* and *Paper VII*, where the effect of turbulent diffusion on MRI is examined. This is the case, in particular, with galactic disks, where energy input of SNe is dominant. Although the signatures of MRI are not manifested in the local DNS models of SN-driven turbulence (see e.g. Gent et al., 2013a;

Bendre et al., 2015) with parameters describing the solar neighbourhood, this does not completely rule out the relevance of MRI in galaxies, as the SN rate diminishes as a function of radius (Ferrière, 2001).

The study of Sellwood & Balbus (1999) estimated the velocity dispersion in extended HI disks around spiral galaxies, and found out that it is remarkably uniform. As there is no stellar forcing available in the HI disks, which indicates that another source of turbulence is needed. As a potential source of such velocity dispersions, they proposed the MRI. To investigate whether such a scenario is possible, in *Paper I* we elaborated on extending the MRI damping condition found from the linear stability analysis into the Milky Way conditions. We estimated the turbulent diffusivity as function of the galactic radius by using the first-order smoothing approximation (FOSA; Steenbeck et al., 1966), into which the estimates of turbulent velocities and scales were fed in from some numerical models (Dib et al. (2006) for velocity dispersion as function of SN rate; Korpi et al. (1999c) for the typical length scale of turbulence). As a result, we found out that SNe dominate over MRI up to roughly 13.6 kpc distance from the centre. This estimate has been verified later by hybrid simulations of the ISM including differential rotation and SNe (Gressel et al., 2013). Therefore, we expect that the scenario proposed by Sellwood & Balbus (1999) is viable. We also note that, with sufficiently high rates of rotation, particularly, in the cold phase gas and/or within the limits AKA-estimate of turbulent viscosity, the damping condition for MRI is not fulfilled, as depicted in the Figure 12 of *Paper VII*.

4.2.2 Supernova-driven turbulence

SNe are significant contributors of thermal and kinetic energy to the ISM. Energy released by a single supernova is immense, approximately $\sim 10^{51}$ erg (Ostriker & McKee, 1988; Khokhlov et al., 1993). Of that about 5-10% is released as kinetic energy, and the rest dissipates through radiative cooling (Chevalier, 1977; Korpi, 1999). Korpi (1999) lists four dynamically important energy inputs into the ISM. Weakest of these it the large-scale shear, with energy flux of $10^{-4}\,\mathrm{erg\,g^{-1}\,s^{-1}}$, which means that even discounting turbulent diffusion other sources of energy will be more important to the total dynamics of ISM. Both stellar radiation pressure and stellar winds have the energy flux of $2 \times 10^{-3}\,\mathrm{erg\,g^{-1}\,s^{-1}}$, which gives them dynamical significance. However, SNe produce the most intensive energy flux, $4 - 8 \times 10^{3}\,\mathrm{erg\,g^{-1}\,s^{-1}}$, showing them to be one of the most forceful mechanisms in driving ISM turbulence, and therefore integral part of the galactic dynamo.

Multiphase stucture

Many studies of SN-driven turbulence (Cox & Smith, 1974; McKee & Ostriker, 1977; Korpi et al., 1999b; Gent et al., 2013a) have argued that SNe have an important role in creating a multiphase interstellar medium, in particular its hot component which fills up almost half of the ISM volume. The multiphase ISM can be divided into three characteristic phases: hot, warm and cold. These phases emerge as a combination of SN heating, radiative cooling and mixing by SNe.

The hot phase ($T \simeq 10^6$ K) is produced by the energy input from SNe, and according to Gent et al. (2013a) it dominates the regions away from the galactic midplane, while other phases dominate the midplane itself. Near the midplane, by the volume filling factor, most of the ISM is in the warm phase ($T \simeq 10^4$ K), however most of the dense matter is distributed in the cold phase ($T \simeq 100$ K), which is the domain of the molecular clouds.

The hot gas flows tend to create a galactic fountain effect (Bregman, 1980). SN-driven turbulence creates an outflow of hot gas in the direction of the galactic halo. There, the hot coronal gas cools down and rains spiralling back towards the galactic midplane.

Apart from SNe, the three phases are formed by a combination of photoelectric heating and radiative cooling (Wolfire et al., 1995). The properties of the radiative cooling function are such that in a certain temperature range, thermal instability occurs (see e.g. Gent et al., 2013a, Table D1). In the absence of the hot phase, such as in the two-phase picture of Field et al. (1969), gas in the unstable regime cools rapidly, and due to this contracts and forms clumps until they reach another stable state of higher density and lower temperature. The surrounding stable, warmer and less dense gas forms another, more diffuse, phase around the clouds. Supernova mixing pushes gas away from these discrete stable states and a lot of gas exists in the unstable rage, too. However, the interface between cold and warm/hot phases is a widely discussed scientific question (Elmegreen & Scalo, 2004) and the effects of large scale turbulence to small scales should be examined in more detail.

Nature of SN-driven turbulence

Each SN explosion is initially purely potential. If homogeneous surrounding medium is assumed, divergence of the flow is non-zero, shock front expands radially and vorticity vanishes. The explosion fronts expand with velocities exceeding the sound speed of the surrounding medium, and therefore strong shocks are formed. However, a purely potential flow does not produce the desired results. Observed ISM turbulence follows a Kolmogorov-like power spectrum (Armstrong et al., 1981, 1995) ($\propto k^{-11/3}$). A spectral slopes -3 for solenoidal and -2 for compressible flows would be expected (see e.g., Vazquez-Semadeni et al., 1995, and references therein). As the SNe are the dominant source of turbulence in the ISM, and as the observed power spectrum fits better with the solenoidal slope, there is an indication that the turbulent interstellar flow produced by an ensemble of these explosive events would posses significant amounts of vorticity.

According to the Kelvin–Helmholtz theorem, vorticity is a conserved quantity in many flows, but there are some conditions which violate this (see e.g. Chernin, 1996). These include shocks, helical forcing, viscosity and baroclinicity – all of which are a part of ISM turbulence. However, only numerical investigations of the full system will provide answers as to which of these effects, if any, can be responsible for generating large amounts of vorticity in the ISM.

The early numerical results of Korpi et al. (1999a) of SN-driven turbulence in local domains gave the first indications that this is indeed the case – efficient vorticity generation was observed, and this was mainly linked to the baroclinicity and the stretching of vortex

lines. The simulations were, however, of low resolution, and all the terms in the vorticity equation were not systematically monitored, leaving many open questions. Among these were the importance of rotation and shear, also included in the model.

The next study of SN-driven flows paying attention to this problem were the self-gravitating AMR simulations of Padoan et al. (2016b); Pan et al. (2016); Padoan et al. (2016a, 2017) that, however, excluded any large-scale effects such as density stratification, rotation, and shear. They also did observe large amounts of vorticity being generated, ruling out any major role that rotation and large-scale shear could have had in the early results of Korpi et al. (1999a). They did not, however, systematically study how the vorticity was generated in the system, but based on qualitative arguments, proposed that the vorticity has to result from baroclinicity originating already at the time of injection due to the inhomogeneities in the surroundings. Iffrig & Hennebelle (2017) have examined the occurrence of baroclinicity in their respective models, but they did not witness significant vorticity generation, which might be explained by their model did not include thermal injection. Instead they modelled SNe with pure momentum injection.

In *Paper VII* we undertook an attempt to perform such analysis, again including the full ISM setup similar to Korpi et al. (1999a), monitoring all the terms in the vorticity generation equation. The most notable differences to Korpi et al. (1999a) were the scheme of how to set off SNe being dependent on the mean density versus the earlier results having a totally random horizontal distribution, and some subtle differences in the scheme for numerical diffusivities. As a result, we found that baroclinicity is, indeed, the dominant source of vorticity, and that the vorticity generation can be attributed to the expanding SNe and superbubbles that the clustered SN activity generate. Vortex stretching was found to generally act as a sink of vorticity, in contrast to the earlier results of Korpi et al. (1999a). Locally, especially outside the SN bubbles in the denser and cooler gas, vortex stretching could act as a source of vorticity, these two vorticity generation regions being clearly separated. The random SN distribution of SNe in Korpi et al. (1999a) could explain the differences between these studies, as with such forcing no superbubbles can actually form, and therefore the dynamics of the system is quite different.

The results obtained for SN-driven systems, therefore, suggest that rotational modes dominate over the compressible ones against the common assumption of isothermality and purely compressible forcing (see Mac Low, 1999, as a well known example). In appears that, a realistic ISM model should consider taking the baroclinicity and its consequences into account. Also, in those models where smaller scales effects are studied, and where interstellar turbulence has to be modelled by generating parameterised descriptions either to be used as an initial condition or as a forcing function, consideration for baroclinicity could prove to be interesting.

In *Paper VI* we also studied the probability density functions of the velocity and magnetic fields of the magnetohydrodynamic simulation data of Gent et al. (2013a,b) to examine the common hypothesis of the distributions being Gaussian, as assumed at least in Planck Collaboration Int. XXXII (2016), Soler et al. (2016), Planck Collaboration Int. XLII (2016) and Planck Collaboration Int. XLIV (2016), Planck Collaboration Int. L (2017). As a result, we found that the velocity field is non-Gaussian with extended wings,

and therefore conclude that the SN-driven flow is highly intermittent – at least in the dominant warm and cold phases. Also, the magnetic field distribution was non-Gaussian, disagreeing with the widely used assumption that fluctuations in the interstellar magnetic field can be functionally randomized assuming a Gaussian distribution, as in the above references. The result of does not invalidate the studies mentioned above as such, but suggests that assuming Gaussianity might not be the best approximation – particularly with diffuse ISM.

4.3 Consequences of turbulence: connections between scales

4.3.1 From large to small scales

A characteristic type of behaviour of a turbulent system is its energy cascade. The larger scale turbulence passes on energy to the smaller scales until the dissipation scale, set by the diffusivities is reached. The most famous law for the turbulent cascade is the Kolmogorov energy spectrum

$$E(k, \epsilon) = C\epsilon^{2/3}k^{-5/3} \tag{4.3}$$

where C is a constant, ϵ is the energy dissipation rate and k is the wavenumber. However, the Kolmogorov spectrum holds for incompressible, homogeneous and isotropic fluid, which is not really corresponding to the ISM.

Iroshnikov-Kraichnan scaling (Iroshnikov, 1964; Kraichnan, 1965) is a similar kind of scaling relation where $E(k) \propto k^{-3/2}$, which is derived for compressible MHD turbulence. Due to SN-driven strong shocks, even a steeper power-law could be expected (Vazquez-Semadeni et al., 1995). However, even this relation does not necessarily hold for multiphase ISM on all scales. Discussion of the proper power-law relation – if such exists – has been extensively reviewed by e.g. Elmegreen & Scalo (2004) and Korpi (1999).

The existence of a unique power-law behaviour is challenged by the complexity of processes involved in interstellar turbulence. Firstly, there are various processes providing forcing at various scales (shear at large scales, SNe at intermediate scales and for instance thermal instability at molecular cloud scales) making the starting point of the cascade ill-defined. Moreover, some processes carry energy to both directions such as SNe, which transfer energy first to larger scales as they expand. During the expansion in the inhomogeneous medium, further mixing at smaller scales than the expansion front itself occurs. Some of this energy cascades to smaller scales and some of it can drive instabilities that cause an inverse cascade, such as a dynamo.

Observationally, however, the cascade appears appealingly simple: the interstellar scintillation observations by Armstrong et al. (1995) show that the turbulent fluctuation in the ISM follow Kolmogorov-like ($\propto k^{-11/3}$) scaling over a vast range of distances. Firstly, the existence of a power-law scaling is surprising in itself taken the flow complexity.

Secondly, the power index being close to Kolmogorov scaling is unexpected, as discussed above, if the dominating forcing is a shocked SN flow.

At the scale of the molecular clouds, SNe can be thought to affect the process through three routes.

1. Providing source of turbulence cascading from larger scales mixing the ISM where molecular clouds are embedded.

2. When occurring in the vicinity of a star formation region, triggering star formation by their expansion fronts.

3. Through dynamo-generated magnetic fields, both at small and large scales, that they participate in generating.

It is extremely challenging task to make a model including all effects (1,2,3). This thesis contributes mostly to 3) by resolving scales small enough to enable small-scale dynamo (SSD) action while retaining large enough scales to enable large-scale dynamo (LSD) action and to 1) providing means to characterize SN forcing properties to be included in a smaller scale model. There are some other models, such as Padoan et al. (2016b) and Iffrig & Hennebelle (2017), who have contributed to 1) with models that cannot address 3). In that sense, the modelling efforts are not yet directly useful when tying together all the scales and their interactions.

At the scales of molecular clouds

Our observational efforts in this thesis have focused on the scale of cold cores, which are the most compact parts of molecular clouds. In our SNe models, the cold phase, which is the scale of giant molecular clouds (GMCs), is barely resolved. Therefore, what can be found in between these scales warrants discussion (see Fig. 4.1 for reference).

The choice of non-overlapping scales between the numerical and observational studies was a compromise that we had to make on one hand to reach our most important goal of including the dynamo process and the relevant inverse cascades in our models, on the other to keep the computational time requirements within the limits of the available resources. Naturally, the modelling strategy of the cold phase needs to be improved, and in Chapter 8 we list the avenues foreseen in the near future.

The size of GMCs range approximately between $10 - 100$ pc, with masses between $10^3 - 10^5 \mathrm{M}_\odot$ (Murray, 2011). The modelling of these structures is, therefore, not so far out of reach resolution-wise, but requires another significant improvement to the used solver. Namely, self-gravity should be included, but the Poisson solver needed for its implementation is currently working only for periodic domains.

GMCs consist of smaller substructures of clumps and filaments (e.g. Alves de Oliveira et al., 2014; Heyer & Dame, 2015). The smaller clumps and prestellar cores are found within gravitationally unstable filaments, and more massive cores and star clusters are often found in the filamentary intersections. Alves de Oliveira et al. (2014) also note that the observed turbulent properties of the different GMCs in connected cloud complexes do

not show characteristic local differences. This implies that the clouds are impacted by a common large-scale process, and indicates that SN-driven turbulence (or other turbulent forcing mechanism working on a larger scales than the clouds themselves) could have a great influence on GMCs. This could be interpreted to indicate that complete understanding of star formation will require an informed comprehension of turbulence on large scales, even though other effects like gravitation are also influential (see e.g. Ibáñez-Mejía et al., 2016).

Turbulent structure of GMC filaments can be investigated using molecular line observations. The observation of Schneider et al. (2010) of DR21 filament implies that such filaments are formed by the convergence of large-scale flows which has further lead to gravitational collapse. Their measured molecular line dispersion show that the turbulent velocities slow down towards the filament's centre.

The large filament of Schneider et al. (2010) also shows subfilaments. The radial velocity maps of the system imply that the flow along the subfilaments is converging into the main filament, and the flow is aligned with the estimated magnetic field direction. Similar kind of subfilament behaviour have also been observed with Herschel Space Observatory in B211 filament by Palmeirim et al. (2013), where subfilaments suggest to accrete mass into the main filament. A comparable picture is also given by Malinen et al. (2016), who analyse the cloud L1642 with both Planck and Herschel observations. They also note that there is infalling (or flowing out) matter observed towards the dense clumps within the filaments. These kind of cold dense clumps are discussed in the Chapter 5.

The Planck satellite has produced useful information concerning the filamentary molecular clouds and their estimated magnetic field orientations. Planck Collaboration Int. XXXII (2016) has made estimates of magnetic field orientation and molecular clouds on high galactic latitudes. The observed structures show preferential alignment with the magnetic field, where the diffuse medium is more likely to be aligned parallel to the magnetic field whereas dense molecular cloud filaments are shown to have perpendicular alignment with the field. In addition, Planck Collaboration Int. XXXIII (2016) have performed a more in-depth analysis of the Musca, B211, and L1506 filaments, which show that the filaments are aligned in perpendicular direction compared to the estimated mean magnetic field, and also Soler et al. (2016) show such behaviour. Soler et al. (2013) describes a potential scenario for the field orientation: when the magnetic field is strong relative to the gravitational pull, then a molecular cloud is inclined to collapse parallel to the large-scale magnetic field while the field can resist the perpendicular collapse. The resulting collapsed cloud would then be elongated perpendicularly to the large-scale field, as observations seem to indicate.

While in our SN-turbulence model cannot resolve gravitational collapse on the molecular cloud scales, SNe are still driving the formation the large-scale fields. To extend the analysis, it would be possible to isolate the dense cold clumps of the ISM, estimate their gravitational potential in relation to the magnetic field direction and internal pressure – even without implementing full Poisson equation solver for self-gravity during the MHD simulation itself. Therefore, if the scenario of Soler et al. (2013) is correct, these in turn could be used to calculate the preferential molecular cloud alignment. This would make it

possible to estimate the large-scale magnetic field ordering mechanism in relation to the GMC filaments without re-scaling of the turbulence model.

4.3.2 From small to large scales

In addition to the energy cascade from large to small scales, the ISM in galaxies is known to be capable of some self-organizatory processes that transfer energy from small to large scales. This is sometimes called an inverse cascade, and in a sense describes how order can rise from chaos. In the scope of this theses, two of such processes have been studied, namely the galactic dynamo and the emergence of large-scale flows.

Generation of mean magnetic fields

The ISM turbulence takes part also in the generation and maintenance of magnetic field – namely the galactic dynamo (Beck et al., 1996; Beck, 2016). A dynamo is a mechanism that amplifies a weak seed field up to dynamically significant strengths and maintains it over time against diffusive effects. If there was no dynamo, the magnetic field would eventually dissipate and disappear. However, dynamically significant magnetic fields are observed in galaxies (Beck, 2016), this implies that some re-generative process is needed to compensate for the enhanced decay of the magnetic fields due to the vigorous turbulence.

A galactic dynamo can exist in a situation where the inductive processes dominate over the diffusive ones. The type of the dynamo can be envisioned to be either a helical turbulent dynamo driven by SN-forcing (as in the models of Gressel et al. (2008) and (Gent et al., 2013a), the latter data of which was used in *Paper VI*) or a MRI dynamo or both localized at different radii (*Paper I*, Gressel et al., 2013).

A common method to investigate the dynamo mechanism is through the mean field theory (e.g. Rädler, 1980). In mean field theory, the velocity and magnetic fields are divided into the mean component and the fluctuating component,

$$\mathbf{U} = \overline{\mathbf{U}} + \mathbf{u} \quad \text{and} \quad \mathbf{B} = \overline{\mathbf{B}} + \mathbf{b}. \tag{4.4}$$

These expressions are substituted into the induction equation and the separate evolution equations are derived for the large and small scale quantities. The large-scale equation thereby obtains a term that contains turbulent correlations. This is called the mean electromotive force $\epsilon = \langle \mathbf{u} \times \mathbf{b} \rangle$, and it essentially describes the collective inductive action of the turbulence and also the enhanced turbulent diffusion due to the efficient mixing. In a system where turbulence is such that the emf is non-zero, the turbulence can thereby participate, together with differential rotation fed into the system through $\overline{\mathbf{U}}$, in generating magnetic field at the largest scales ($\overline{\mathbf{B}}$), indicative of the presence of an inverse cascade. One such case of turbulence are flows that possess helicity.

In addition to the generation of magnetic fields at large scales, the observations show that there is a strong fluctuating component in the ISM, reaching even stronger values than the mean field itself (e.g. Beck, 2016). The fluctuating field is strong in the star-forming regions in the spiral arms, indicating that the stellar component, such as the

SNe (Ferrière, 1996), participates in the generation of it. A part of the fluctuating field can be produced by tangling the turbulence of the large-scale field generated by the LSD. There is, however, growing evidence that the fluctuating fields are generated by a separate process, called the small-scale dynamo (SSD). SNe have already been shown to produce a SSD-active flow by Balsara et al. (2004), who studied a numerical setup where all the ingredient of the LSD were taken out, and SNe were made to explode and interact in a triply periodic cube of compressible gas. There, an exponential growth of the fluctuating magnetic field can be seen, inconsistent with tangling of the initial weak uniform seed field, indicative of the presence of a separate dynamo instability. Such an exponential growth of magnetic field fluctuations is also seen in the model of Gent et al. (2013b). It seems likely that in galaxies such as the Milky Way, LSD and SSD work together, and SN-forcing can act as a source for both effects.

Generation of mean flows

The vorticity equation, which can be derived from the Navier-Stokes equation written for velocity, shares several similarities with the induction equation (Eq. 2.4) Therefore, one would expect that large-scale vorticity could be driven by effects analogous to the ones that cause dynamo action. While several successful examples of dynamos both on large scales (Gressel et al., 2008; Gent et al., 2013a,b) and small scales (Balsara et al., 2004; Gent et al., 2013a,b) have been found from the DNS models of the ISM, even though the net helicities are relatively weak, an analogous effect of generating mean flows has eluded us until *Paper VII*.

In the runs presented in the *Paper VII*, generation of large-scale horizontal vorticity, and the resulting appearance of z-dependent mean horizontal flows, occurs. The flows are oscillatory and the period of oscillation depends on the rotation and shear rates. We interpret these flows to arise as a result of an anisotropic kinetic α (AKA, see e.g. Brandenburg & Rekowski, 2001) effect which, for the first time, was detected in a natural setting. The existence of this effect in our models provides another example of the inverse cascade in the ISM.

5 Early stages of star formation

In the previous chapter, the turbulent effects on relatively large scales were discussed. However, when looking downstream towards smaller scales, where denser cold cores within large molecular clouds are seen, star formation process itself becomes an issue. These cold cores, representing the early stages of star formation, were investigated in *Paper II* and *Paper III*.

Paper II discusses the cold core object, Ophiuchus D (L1696A). Oph D is a core clump connected with the larger ρ-Ophiuchi molecular cloud complex, which is located relatively close by (119 ± 6 pc, Lombardi et al., 2008), and the main cloud contains several dense cores and candidate young stellar objects (Motte et al., 1998). *Paper III* features a cold core, Chamaeleon-MMS1, which is contained in a GMC called the Chamaeleon I dark cloud. Whittet et al. (1997) gives Chamaeleon I the size of 160 ± 15 pc and mass $10^3 - 10^5 \mathrm{M}_\odot$. Also with Chamaeleon cloud complex, there is known presence of active star formation, although Chamaeleon I is seen to be past its most active star formation phase (Alves de Oliveira et al., 2014).

5.1 Cold cores

The cold cores represent some of the densest parts of the ISM. They are gravitationally bound and also show signs of turbulence in their observed velocity dispersion (Bergin & Tafalla, 2007). Cores can be condensations within larger clouds, potentially separated by turbulent fragmentation. While some of the cold cores manage to stay stable in hydrostatic equilibrium, at least temporarily, radiative cooling and interaction with the surrounding medium can push them over the Jeans limit and lead to a collapse into a star (McKee & Ostriker, 2007).

In this equilibrium state, the core is commonly approximated with Bonnor-Ebert sphere (Ebert, 1955; Bonnor, 1956) (BE-sphere). This describes the structure of the cloud as an isothermal, hydrostatic sphere in embedded in pressurized surrounding medium ($2E_{\mathrm{kin}} + E_{\mathrm{grav}} = 3P_{\mathrm{out}}V$). There exists also more complicated implementations of BE-spheres. For example, Sipilä et al. (2011) have examined the stability of a non-isothermal BE sphere that has a radial temperature gradient owing to the attenuation of the interstellar radiation field.

However, considering the turbulent nature of the ISM, BE-sphere is an approximation. While it provides suitable fits to several observations (Bergin & Tafalla, 2007),

there should be no reason to assume that such approximation describes the core over long timescales. However, BE-sphere approximation is useful as an initial condition for dynamical models or as a basis for astrochemical models where dynamics cannot be easily implemented. Like in the case of *Paper II*, BE-spheres are utilized in its analysis, both for an astrochemical model or as the initial condition for the rotating spheroid model.

5.2 Stages of star formation

If gravitational instability drives a cold core into collapse, the process of star formation begins. This process can be divided into a number of stages. The initial cloud collapse progresses by approximately radial compression of the core dragging and rotationally twisting the magnetic field within it (Machida et al., 2008), with a possible influence from turbulent dissipation, weakening the magnetic braking Joos et al. (2013).

During the core collapse, the system can reach a point where the internal pressure of the collapsing core is able to oppose further collapse. This is known as the first hydrostatic core (FHSC) stage (Larson, 1969). However, the FHSC stage has not been identified with direct observations so far. There are only a few very low luminosity objects (VeLLO) which are FHSC candidates. To get a sense of VeLLO and FHSC candidates, a recent article by Maureira et al. (2017) lists several of these candidates in their introduction. Chamaeleon-MMS1 featured in the *Paper III* is one of them (Belloche et al., 2006).

After the FHSC stage, the star formation process becomes more visible. A following observational classification can be presented for the early stages (Barsony, 1994; Andre et al., 2000).

- *Class 0* objects radiate most of their luminosity at far-infrared and submillimetre wavelengths, and faint mid-infrared emission from the central protostar is detected. Such early protostellar objects have thick envelopes, which show rotational velocity profiles (Tobin et al., 2010, 2011, 2012).

- *Class I* objects are detectable in the near-infrared. The spectral energy distribution (SED) shows an increasing flux density longward of 2.2 μm, up to about 100 microns. The spectral index, $\alpha = -d\,\log(\nu S_\nu)/d\,\log(\nu)$, is positive in this range (ν is frequency and S_ν is the flux density). In Class I objects, the central protostar is surrounded both by an envelope and by a circumstellar disk.

After these early stages, the process will continue toward the eventual dispersion of the protostellar envelope, the circumstellar disk and the end of star formation.

5.3 Outflows from circumstellar disks

One of the most visible phenomena concerning the magnetic field during the cloud collapse are protostellar outflows. As the angular momentum is conserved in the cloud collapse, the rotation of the star-forming core twists the compressed magnetic field. The process

creates high magnetic tension in the field, and because of this, part of the infalling matter and energy escapes the system through a bipolar outflow (Machida et al., 2008). These magnetocentrifugal winds occur because the angular momentum can only escape through open poloidal field lines, when the disk is dominated by toroidal magnetic fields (Blandford & Payne, 1982). The magnetocentrifugal acceleration has also been developed into more refined models, such as the X-winds where the magnetic interaction between a central protostar and a disk can induce a collimated outflow (Shu et al., 1994, 2000).

It is possible to find molecular outflows starting early on, perhaps already at the FHSC stage. If we follow the basic principles of the scenario presented by Machida et al. (2008), when the cloud has collapsed into a FHSC, the magnetocentrifugal acceleration can produce already at this stage a widely spread, slow ($\sim$ 30 km/s) molecular outflow. Later, after the FHSC stage, the outflow turns into a well-collimated, fast outflow ($\sim$ 100 km/s). However, molecular line emission (such as CO and NH_3) related to outflows can also represent ploughed away gas around any general outflow (Bachiller et al., 1993; Arce & Sargent, 2006). Especially during the early stages of star formation, the exact mechanism for molecular outflow formation is unclear, unless faint early outflows can be detected, for example with ALMA. However, there are a few early observed outflows from VeLLOs (e.g. Dunham et al., 2011), which hint at the possibility of FHSC stage outflows.

Later in the process, the outflow becomes hot and bright enough to be observed in optical wavelengths (Hayashi et al., 1996; Chini et al., 1997). These extended outflows can emerge as Herbig-Haro objects showing signatures of ionized, shocked outflow gas (Lada, 1985; Reiter et al., 2017).

The potential presence of an outflow in the prestellar core Cha-MMS1 was one of the central questions discussed in the *Paper III*. The radial velocity distribution of the core gave us a suspicion of an early stage outflow, and we found some circumstantial evidence for the scenario. First, a two-component fit made to the observed $NH_3(1,1)$ emission indicated, that along the approximate central axis of observed core rotation the ammonia had higher excitation temperatures. Second, this distribution overlaps the region showing 1.2 cm continuum emission and $NH_3(2,2)$ wide band emission. However, this circumstantial evidence does not give a definite answer to the question. For that, other high-resolution observations are required.

In a cluster of forming stars, where the protostellar objects are relatively nearby each other, the outflows can even affect their neighbours – the neighbourhood of Chamaeleon-MMS1 being one example. It has been shown by Hiramatsu et al. (2007) and Ladd et al. (2011) that a molecular outflow from the neighbouring IRS4 protostar is colliding the Chamaeleon-MMS1 core, creating an exotic situation yet to be fully explored.

5.4 Connection to large-scale turbulence

Chapter 4 argued that in a turbulent flow, all scales are connected either through an energy cascade from large to small scales, or through an inverse cascade from small to large scales. In that sense star formation also functions in a turbulent system, and the parametrization of the turbulence is highly non-trivial. When the effect of turbulence

on cloud collapse is studied, a common approach is to generate a small-scale turbulent field as an initial condition with various assumptions about its power spectra (e.g. Joos et al., 2013; Li et al., 2014; Seifried et al., 2016). Some recent studies do not even include turbulence in their models (e.g. Machida et al., 2016).

Setting turbulence as an initial condition can be a reasonable approach, given the limits of computational resources required, and that the research question might require limiting the work into a certain parameter space. However, the maintenance of turbulence in a system requires a driving mechanism, otherwise, the velocities and magnetic field are dampened by diffusivities. So far no mechanism of core-scale turbulence driving has been implemented by any core collapse model that explores protostellar formation process.

The choice of a turbulent field is not irrelevant. Joos et al. (2013); Seifried et al. (2016) observed that turbulence reduces magnetic breaking efficiency during a cloud collapse; making disk formation more efficient. Also, Li et al. (2014) saw that turbulence had considerable influence on their pseudo-disk formation. The initial turbulence has been also found to induce a SSD in collapsing clouds (Sur et al., 2010; Federrath et al., 2011), and it can affect fragmentation the collapsing core into multiple stars (Offner et al., 2016). Whatever assumptions are made for the initial condition or driving mechanism for turbulence, they will influence the results at later stages in the cloud collapse models, in yet little-explored ways.

Models of SN-driven turbulence provide estimates on how the velocity and magnetic fields are structured in the ISM in the parsec-kiloparsec scales. In *Paper VI*, we find that the probability distribution function for the magnetic field is exponential/Laplacian, and the velocity field follows primarily a non-Gaussian distribution with extended wings, indicative a strong intermittency in the flow. Such estimates could be used to construct a set of forcing functions to drive turbulence during the star formation process in future work. A forcing function is unable to describe the full turbulent cascade, but it would be relatively inexpensive in terms of computational resources, and an improvement from a mere fluctuating initial condition.

Also, the larger-scale turbulence modelling could be extended towards smaller scales all the way down to the molecular cloud cores by utilizing special computational strategies. This could be done, for example, by scaling down to smaller scales based on larger-scale turbulence models such as Gent et al. (2013a,b) or by AMR simulations such as Padoan et al. (2016b). With AMR models, the method is flexible in adapting to different scales, but the related costs in computation do not allow for the generation of a self-consistent galactic dynamo. With non-AMR models, a self-consistent dynamo is possible, but looking into smaller scales will require refining a subdomain into finer spatial resolution, and will demand intelligent use of boundary conditions. With such approaches we could study how SN-driven turbulence affects the star formation process.

6 Simulating the polarization of galactic dust

In this chapter, discussion on the dust polarization calculations with the continuum radiative transfer code SOC is expanded. Of particular interest are issues concerned with interpretation of large-scale polarization presented in *Paper VI*.

6.1 Radiative transfer with dust polarization

The procedure for using SOC for polarization calculation goes through the following workflow:

1. *Initialization*: Snapshots of density and magnetic field (produced by Gent et al., 2013a,b) are imported and converted into a form readable by SOC. Similarly, a stellar radiation field is set up, based on a simple inversion of Mathis et al. (1983) results.

2. *Emission and absorption*: Emission of stellar radiation and absorption of the radiation by dust is simulated using a Monte-Carlo method (Juvela, 2005). Once these are calculated for every frequency channel, dust temperature can be determined for each cell in the computational domain. The primary calculations are performed with a GPU using OpenCL kernels, where the calculation of travelling photon packages is parallelized with OpenCL threads.

3. *Dust emission*: When the dust temperatures are calculated, the emissivities of each cell per frequency channel are calculated. These values can be used as the basis for the synthetic observations.

4. *POV radiative transfer I*: Radiative transfer equation is integrated along the line of sight with a chosen resolution. Resolution and the indexing of the synthetic observation map has been done according to the HEALPix [1] convention. This sets the resolution as $N_{\rm pix} = 12 \cdot N_{\rm side}^2$ distributed over the whole sphere. In this case, $N_{\rm side} = 512$, making the image oversampled with $\theta_{\rm pix} = 6.'87$ angular resolution (Górski et al., 2005). In this configuration, the result is a projection onto a sphere.

[1] `http://healpix.jpl.nasa.gov/`

We use this spherical all-sky projection, because a kiloparsec-scale domain is dependent on the viewing angle, as well as because we compare our results with Planck Collaboration Int. XIX (2015) observations, which were traced over the whole sky with sufficient signal-to-noise ratio.

5. *POV radiative transfer II*: Based on the magnetic fields and relations presented in *Paper VI*, emission can be divided into Stokes I, Q and U components, and included into the radiative transfer integration. After the calculation, the resulting (oversampled) image is smoothed by a Gaussian kernel function into the preferred resolution (in this case 1° to match the Planck Collaboration Int. XIX (2015) analysis).

6. *Output*: The synthetic observation is saved into a file using a HEALPix indexing scheme (Górski et al., 2005), which can the be analyzed with helpful tools like `Healpy`[2].

While the basic process is straightforward, there are some limitation with regards to the model. One of them is that the domain size of the MHD-model limits the distance up to which the radiative transfer can be reasonably calculated. In addition, with 4 pc spatial resolution we cannot resolve molecular cloud scales in detail. Also, we approximate the degree of polarization with a constant within the simulation cells, which does not take intricacies of radiative grain alignment (Pelkonen et al., 2009) into account. That said, the results of, for example, Planck Collaboration Int. XX (2015) suggest that most variation in polarization degree is due to fluctuations in the magnetic field. We also encounter the challenges with interpreting the projection on a sphere, although this is an issue which is similarly relevant to actual observations of diffuse medium.

6.2 Connecting theory and observations

The purpose of our radiative transfer simulation is, on one hand, to try to validate a SN-driven dynamo model against observations, and on the other, to provide potential explanation for observed phenomena. Since, on the scale of the diffuse interstellar medium, the dust is optically thin, the observed polarization is a combination of emission from large distances, and therefore physical phenomena and their observational correspondences are not always direct. However, producing synthetic observations based on physical justifications can help to make connections which are otherwise less than obvious. The models presented in *Paper VI* are motivated by two primary factors. Firstly, SN-driven turbulence models with various saved full system states were available from Gent et al. (2013a,b). Secondly, the high-quality large-scale observations by Planck (Planck Collaboration Int. XIX, 2015) provide an observational comparison with the modelling results.

The theoretical MHD model behind *Paper VI* was not built specifically for the purpose of explaining Planck observations, for example by intentionally generating a particular

[2] `https://github.com/healpy/healpy`

effect with a turbulent forcing function, and thus it yields an independent test for the theory. This makes *Paper VI* rather special in content, as there has been a variety of studies discussed, which fit the large-scale polarization observations by Planck with a phenomenological or statistical model. Instead, our computed turbulence model started from physical first principles, using numerical techniques.

Planck Collaboration Int. XLII (2016) have interpreted Planck large-scale polarization with a static magnetic field model. They use a selection of models for ordered and fluctuating magnetic fields in our galaxy, and try to estimate new parameters based on the Planck polarization observations and synchrotron emission. However, they suggest that the proper interpretation of the result would require more sophisticated modelling of the magnetic field. In addition, Planck Collaboration Int. XLIV (2016) have built a phenomenological model focusing on the galactic north and south poles, where they produce the distribution of polarization fraction and angle that, according to their judgement, is comparable to the observational results. Also, in this analysis a mean field comparison with a Gaussian random field is used. A way to improve such phenomenological descriptions is to make a consistent dynamo model of the galaxy. This was attempted here with a DNS model which captures the forcing scale and the large-scale field that is induced. The only other model in production usage capable of the same is Gressel et al. (2008).

In connection to Planck, there are several publications which use some form of Gaussian approximation for when generating magnetic field fluctuations for their model fits (e.g., Planck Collaboration Int. XXXII, 2016; Soler et al., 2016; Planck Collaboration Int. XLII, 2016; Planck Collaboration Int. XLIV, 2016; Planck Collaboration Int. L, 2017). However, in *Paper VI* we found that instead of being Gaussian, the general distribution of the magnetic field induced by SN-driven turbulence was exponential in shape, especially in warm and hot phases. Therefore, in future studies, it would be interesting to see how the choice of distribution profile would affect the fitting results, particularly when exploring large scales where diffuse medium play a role.

Our models of SN-regulated ISM can also present how the self-consistently generated three phase cold-warm-hot structure is reflected in observations, despite their limitations of resolution and the lack of extended emission from spiral arms. For the future of ISM magnetism research, if these two very different approaches, namely DNS models of galactic dynamos and methods fitting parametrized models of turbulence with observations, could be brought closer together, there could be possibilities for further fruitful development. However, as neither approach is easy, the unification of both kinds approaches will be a major challenge.

6.2.1 Explaining the major Planck findings

Planck Collaboration Int. XIX (2015) present a number of major findings. They observe:

1. The polarization fraction p and polarization angle dispersion function $\mathcal{S}$ show anti-correlation over the whole sky.

2. Relative depolarization occurs in the direction of the galactic plane.

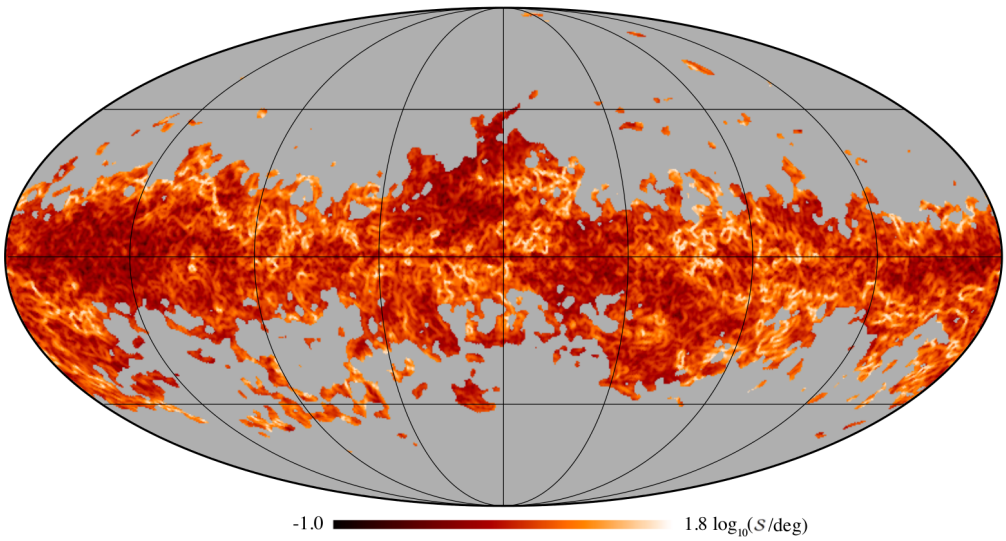

Figure 6.1: *Paper VI* explores the effect of SN-driven magnetic fields on polarized emission. Therein, of particular interest are the polarization angle dispersion ($\mathcal{S}$) observations of the Planck satellite, where $\mathcal{S}$ produces a filament-like structure. (Figure credit: Fig. 12 of Planck Collaboration Int. XIX, 2015, A&A, 576, A104.)

3. Repeating filamentary structures are seen in the $\mathcal{S}$ map, which appear at the borders of the areas which show different but relatively homogeneous polarization angle orientation (See Fig. 6.1).

In relation to these points:

1. Planck Collaboration Int. XIX (2015) suspect that the decrease in polarization fraction is related to the turbulent fluctuation of the magnetic field. Our result and also those of Planck Collaboration Int. XX (2015) appear to agree with the hypothesis, which both produce the anticolleration behaviour. Supporting also the older analysis of Jones et al. (1992).

2. However, in *Paper VI* we also find that there is relative depolarization occurring at the galactic plane of our model, especially at long integration distances. This implies that the depolarization in the galactic plane is also a likely result of from turbulent depolarization over a long distance.

3. The turbulent magnetic field of our model produces $\mathcal{S}$-filaments characteristic to the observations. Planck Collaboration Int. XX (2015) do produce something that can be seen as $\mathcal{S}$-filaments, but their modelling is focused on smaller scales which makes a detailed comparison unreasonable.

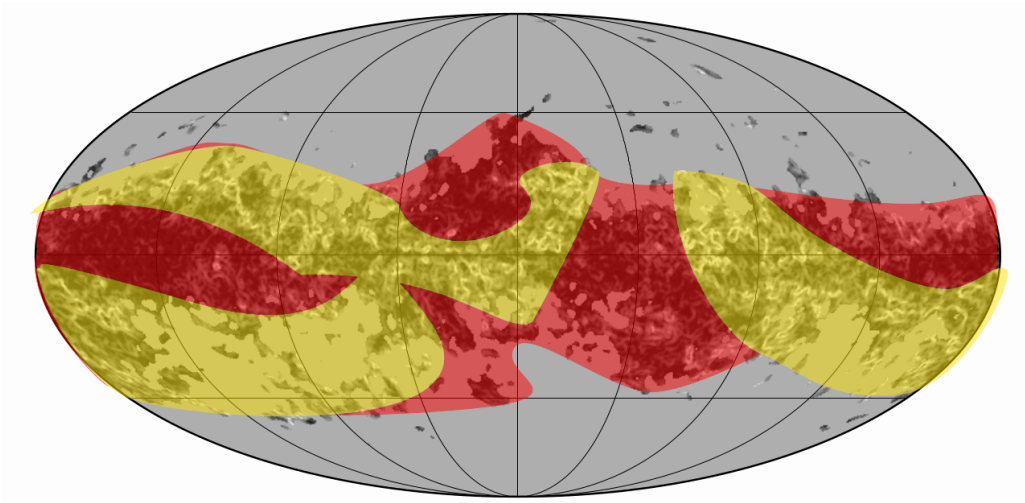

Figure 6.2: A schematic picture of the prediction by the mean field/dispersion connection. According to the hypothesis, the red areas would approximately correspond to the areas with strong POS mean field and yellow areas with strong LOS mean field. (Background figure credit: Fig. 12 of Planck Collaboration Int. XIX, 2015, A&A, 576, A104.)

The $\mathcal{S}$-filaments are not correlated with the shocked regions of the SN-forcing ($C_{\rm shock}$). They can be related to the magnetic field structure in the following way. Our results in the *Paper VI* show that while the characteristic behaviour of the filaments stays similar along different integration depths, the exact shapes of the filaments do not. The $\mathcal{S}$-filaments do not correspond with specific density structures and SNe shock fronts, but they relate to the magnetic field fluctuations along the LOS.

Some behaviour can be interpreted on small and large scales. First, when the polarization angle is affected by the behaviour of the turbulent field, it is prone to show locally coherent behaviour, but it also shows sudden shifts in direction. Therefore, the $\mathcal{S}$-filaments appear in the locations where systematic sudden change in the polarization angle occurs. Therefore, $\mathcal{S}$ has the tendency to mark the borderline of rapid changes in the polarization angle directions, as Planck Collaboration Int. XIX (2015) also demonstrates. Such behaviour could have a number of explanations:

1. The general direction of the large-scale mean magnetic fields at various distances overlap, which would, therefore, show as an apparent change in the polarization angles.

2. There are strong directional changes in the large-scale mean field itself.

3. There are small-scale fluctuations, which acquire a specific direction in polarization when summed over various distances.

Due to the existence of these scenarios, the direct interpretation concerning physical correspondence between the magnetic field and polarization angle will require further study.

On large scales, in *Paper VI* we find evidence that polarization angle dispersion is sensitive to the large-scale component of the magnetic field. If the magnetic field points towards the observer, a higher dispersion is seen and when the strong mean field goes along the plane of the sky the amount of dispersion is weakened. By separating the mean and fluctuating field in the MHD model results, we see that the produced $\mathcal{S}$-filaments are strongly connected to the fluctuating field component. Also in Planck Collaboration Int. XLII (2016), the general patterns in the sky created by the mean field can be seen, but unfortunately their results do not show the estimates for the polarization angle dispersion, which would have been likely outside the scope of their study. Planck Collaboration Int. XX (2015) do also find that the polarization fraction and angle dispersion depend on the angular direction between the observer and the assumed mean field, by changing the angle from which they observe their model.

With all things considered, the following hypothesis could be presented: *If the intensities of the $\mathcal{S}$-filaments are sensitive to the mean magnetic field direction, the general lack or presence of dispersion could function as an indication of the apparent LOS magnetic field orientation in the Milky Way – though only on large scales where mean field effects dominate.* The Figure 6.2 shows a prediction of this simple hypothesis in relation to the Planck $\mathcal{S}$ dispersion map.

The variation in the polarization angle and the existence of $\mathcal{S}$-filaments in the diffuse ISM remain without definite answers even after our study. At least, we have identified avenues of gaining more insights from the large-scale variation in the polarization angle and its dispersion filaments.

7 Summary of the publications

The thesis consists of seven publications:

- **Paper I:** M.J. Korpi, P.J. Käpylä, **M.S. Väisälä**, 2010, *"Influence of Ohmic diffusion on the excitation and dynamics of MRI"*, Astronomische Nachrichten, 331, No. 1, 34-45
- **Paper II:** J. Ruoskanen, J. Harju, M. Juvela, O. Miettinen, A. Liljeström, **M. Väisälä**, T. Lunttila, S. Kontinen, 2011, *"Mapping the prestellar core Ophiuchus D (L1696A) in ammonia"*, Astronomy & Astrophysics, 534, A122
- **Paper III: M.S. Väisälä**, J. Harju, M.J. Mantere, O. Miettinen, R.S. Sault, C.M. Walmsley, J.B. Whiteoak, 2014, *"High-resolution ammonia mapping of the very young protostellar core Chamaeleon-MMS1"*, Astronomy & Astrophysics, 564, A99
- **Paper IV: M.S. Väisälä**, A. Brandenburg, D. Mitra, P.J. Käpylä, M.J. Mantere, 2014, *"Quantifying the effect of turbulent magnetic diffusion on the growth rate of the magneto-rotational instability"*, Astronomy & Astrophysics, 567, A139
- **Paper V:** J. Pekkilä, **M.S. Väisälä**, M.J. Käpylä, P.J. Käpylä, O. Anjum, 2017, *"Methods for compressible fluid simulation on GPUs using high-order finite differences"*, Computer Physics Communications, 217, 11-22
- **Paper VI: M.S. Väisälä**, F.A. Gent, M. Juvela, M.J. Käpylä, 2017, *"The supernova-regulated ISM. IV. A comparison of simulated polarization with Planck observations"*, Astronomy & Astrophysics, Submitted for publication
- **Paper VII:** M.J. Käpylä, F.A. Gent, **M.S. Väisälä**, G.R. Sarson, 2017, *"The supernova-regulated ISM. III. Generation of vorticity, helicity and mean flows"*, Astronomy & Astrophysics, Submitted for publication

The papers are summarised below. The author's contribution to the papers is described at the end of each section.

7.1 Paper I

In *Paper I*, we present an analytical and numerical investigation of MRI damping due to the influence of turbulent diffusion. The question was explored because previous studies

of SN-driven turbulence had not reported any presence of MRI, and also because the Workman & Armitage (2008) gave somewhat contradictory findings that, under some conditions, MRI could be even enhanced due to forcing.

The study is effectively divided into three parts. First, we derive linear stability analysis results for MRI. The analysis is based on Jin (1996) but we generalized it for variable q in the presence of enhanced Ohmic diffusion due to turbulence. The analysis results in a stability condition for MRI, with estimation of turbulent diffusion with the help of FOSA.

In the second part, the results of the linear stability analysis are compared with a non-stratified isothermal numerical model including a shear flow, with added forcing effects to generate external turbulence. The effect of turbulent diffusion on MRI is measured by examining the turbulent stresses on both MRI stable and MRI unstable ranges. MRI stability is achieved by either performing purely hydrodynamical runs of using a negative shear parameter q. The simulation results indicate that turbulent diffusion can weaken the MRI growth.

In the last part, we apply the linear stability analysis results to a radial profile of a galaxy. The results show that MRI is likely suppressed within the inner SNe turbulence dominated region, but might be present in the outer regions of a galaxy with weaker SNe rates.

Author's contribution

The author derived and performed the calculations of linear stability analysis presented in Section 2 of the paper.

7.2 Paper II

Paper II shows the observations of NH_3 (1,1) and (2,2) spectral line from the Ophiuchus D (L1696A), with the Very Large Array (VLA). Oph D is an isolated core apparently fragmented from the ρ-Ophiuchus molecular cloud. As an isolated core, Oph D worked as a case to measure the temperature distribution of a cold core.

The observations were compared with model fits to modified Bonnor-Ebert spheres calculated with corresponding ammonia abundances. The fitting was made with the help of 3D Monte Carlo radiative transfer simulations, and the physical/chemical model was adjusted to fit the simulated emission with the observed core. Also, an alternative spheroid core model was used to examine a potential deviation from a strictly symmetrical BE-sphere.

The observations show that the Oph D contains two separate (northern and southern), potentially prestellar, cores. The cores are observed to show velocity gradient implicating rotational motion, with both cores rotating approximately to opposite directions. BE-model approximated the southern core reasonably well, with temperatures ranging from 10 K on the surface to 6.1 K in the centre. Northern core result indicates temperatures of either 8.8 K for BE-fit or 7.4 K for a spheroid core fit. However, no satisfactory BE-model

fit could be achieved for the northern core, while tentative evidence for a spheroid core providing a better fit was observed.

Author's contribution

The author made the alternative spheroid core model featured in Section 4.2 of the paper by using and modifying the Pencil Code.

7.3 Paper III

Paper III presents NH_3 observations of Chamaeleon-MMS1 cloud core made with ATCA interferometer and 64 m Parkes Telescope. We also utilized data from Spitzer Space Telescope and Herschel Space Observatory for further interpretation of the observations. Cha-MMS1 is a candidate for a FHSC, and therefore represents a rarely observed stage in star formation.

We observed a steep velocity gradient the direction of which is compatible to the previous estimates by Ladd et al. (2011). The estimated angular momentum of the core is typical for protostellar envelopes, and the rotational axis colludes with compact far-infrared sources observed with both Spitzer and Herschel. Also, a tentative string of 1.3 cm continuum sources was detected near the rotation axis. A two-layer model fit to the NH_3 (1,1) spectral lines reveals an underlying component of elevated temperature coinciding with the rotational axis, indicating a source of heating within the core.

The estimate based on fitting the object's SED with prestellar core models suggests that Cha-MMS1 is either at FHSC or Class 0 stage object, but the very low luminosity is more compatible with a FHSC. The continuum observations, the hourglass shape of NH_3 emission at the nominal velocity of the cloud and elevated temperature near the rotational axis all hint towards the existence of an embedded molecular outflow. However, no CO outflow has been detected, which has been the case with other candidate VeLLO/FHSC outflows. The question could likely be resolved with high-resolution N_2H^+ observations with ALMA.

Author's contribution

The author had a major role, in cooperation with J. Harju, in the analysis and interpretation of the Chamaeleon-MMS1 observations presented in the paper. In particular, he contributed to the physical interpretation of the observed molecular cloud core. The author and J. Harju wrote the majority of the paper with helpful comments and contributions from the other co-authors. The author would like to thank, in particular, the helpful and informed comments of C.M. Walmsley during the writing process.

7.4 Paper IV

Continuing with the questions posed in *Paper I*, *Paper IV* examines the effects of turbulent diffusion on MRI, this time looking at the growth-rate during the linear stage. Performing the study this way allowed for keeping the numerical diffusivities simple and minimal for reliability, and made it possible to investigate an extended parameter space.

MRI-active simulations were performed with a quasi-periodic shearing sheet approximation, using turbulent forcing with plane-waves to generate external turbulence. The runs were performed with varying forcing amplitude and wave number, rotation rate and strength of the magnetic field. The turbulent diffusion was estimated using both FOSA and test-field method (for selected runs).

The study shows that the turbulent diffusivity behaves in an equivalent manner to microphysical magnetic diffusivity, even in the case of poor scale separation. In addition, FOSA and test-field estimates of turbulent diffusivity are in reasonable agreement.

Author's contribution

The author designed and performed the MRI simulations and all connected analysis collaborating with A. Brandenburg and D. Mitra during his visit to Nordita in summer 2013 and afterwards. The author took the main responsibility with the paper, with the help of the co-authors.

7.5 Paper V

Paper V we present techniques to accelerate high-order finite difference method with GPUs, and some optimization which the best possible performance and speed up can be achieved. As GPU computing represents a rather novel computing and coding paradigm, we also present and perform various physics tests. Based on these methods we have developed the NVIDIA CUDA based Astaroth code, and the study explains the various methods, algorithms and tests utilized with the code.

We present two methods to handle the FDM stencils on the GPUs, which we denote 19-point and 55-point methods. There an essential difference between the two is how to handle the derivative operation $\nabla(\nabla \cdot \mathbf{u})$, which requires diagonal values to be computed fully. The 55-point method calculates the bidiagonal derivatives directly, while the 19-method separates the calculation into two stages, using only the conventional first and second derivatives.

We find that both methods produce satisfactory results with the physics test cases. The 19-point method is the more efficient approach, with 3.6× speedup in comparison to equivalent Pencil Code run benchmarked with two Intel Xeon E5-2690v3 processors.

Author's contribution

The author created the main system and functionality of the Astaroth code, and physics testing tools that were used. J. Pekkilä contributed by important optimization implementations and performance testing. The paper itself is written with equal contribution from both the author and J. Pekkilä, and the other authors have made important comments and additions to the text. It should be noted that while the development of Astaroth code has only resulted in one published paper so far, the development of it has started already in 2012 and has been the single most time-consuming task in this thesis.

7.6 Paper VI

This paper presents an attempt to build a bridge between numerical models and observations. We perform 3D Monte Carlo radiative transfer calculations of interstellar dust, based on the MHD simulation data of Gent et al. (2013a,b), and produce synthetic whole-sky observations of Stokes I, Q and U components of linearly polarized submillimetre emission of dust. The results are compared mainly with the whole-sky dust polarization maps observed by Planck Collaboration Int. XIX (2015), and other relevant Planck studies.

We find that SN-driven turbulence can indeed produce comparable results to the Planck observations. The synthetic observations produce a similar filamentary structure of polarization angle dispersion function $\mathcal{S}$ as seen in the Planck all-sky maps. However, the smallest scale structures are not visible on our maps. We can reliably rule out that the $\mathcal{S}$-filaments would be directly related to SN-driven shock fronts, and the $\mathcal{S}$-filaments can clearly be attributed to the variation caused by the small-scale magnetic field fluctuations. Our results also support the notion that general intensity fluctuation of $\mathcal{S}$-filaments are influenced by the orientation of the mean plane-of-sky magnetic field, in a way that a strong POS-field weakens the amount of fluctuations while increasing the polarization fraction. Polarization fraction and angle dispersion are anticorrelated, and polarization fraction decreases as a function of column density. We observe also that the fluctuations of magnetic field follow an exponential distribution, rather than Gaussian, which is characteristic of flows influenced by repetitive shocks from SNe.

It is the first time when SN-driven turbulence models with a dynamo-generated magnetic fields are compared with the observed large-scale polarisation of dust. Our findings are rather general, but some details raised in this study may inspire further investigations.

Author's contribution

The author performed and analyzed the results of the radiative transfer simulations made using the SOC code provided by M. Juvela and SN-turbulence data provided by F.A. Gent and M.J. Käpylä. The author made modifications to the SOC code so that the model could include an internal stellar radiation field and produce synthetic polarized emission observations over the whole sky. The author had the main responsibility of the paper, in

cooperation with the co-authors.

7.7 Paper VII

This paper shows the results of hydrodynamical SN-driven turbulence models. Three with positive q, one without rotation and three with negative q. As the model intentionally lacks magnetic field, it is concerned with the turbulence generating processes themselves, and different parameters allow for comparison in terms of influence by both rotation and shear direction.

The results show that 65% of the kinetic energy is distributed to the rotational modes of the velocity field. The vorticity is primarily related to the baroclinicity of the flow, induced by the expansion of overpressured supernova bubbles in the inhomogeneous medium caused by previous SNe, causing misalignment of temperature and entropy. The magnitude of baroclinicity is strong enough to suggest that thermodynamic effects are significant for the dynamics of the ISM. Also, the commonly used assumptions of isothermality and pure compressibility are likely to be unreliable.

The rotation and shear-generated helicities are found to be of opposite signs, with near cancellation of total helicity in the solar neighbourhood. In addition, oscillatory mean flows are generated which, after a careful inspection of the system, we interpret to be a sign of the AKA effect. The method of moments used to measure the inductive and diffusive contributions to the mean flows gave us also an estimate of the turbulent diffusivity. Therefore, we were able to refine our earlier estimates of the MRI damping condition presented in *Paper I*. MRI stability criterion of *Paper I* is also tested using the FOSA and AKA estimates of turbulent diffusivity. We find that while the damping criterion is mostly fulfilled in the models with Milky Way rotation and shear rates, MRI could be possible in more rapidly rotating disks, particularly in the warm and cold phases.

Author's contribution

The author performed the estimate of the MRI damping conditions presented in Section 3.5, and contributed significantly to the writing of the manuscript. He also made Figure 2.

8 Conclusions and future prospects

In this thesis, the properties and dynamics of the ISM have been discussed from multiple perspectives. The work here has also aimed to explore connections between observational and numerical approaches. Two of the papers included in the thesis are concerned with the analysis and interpretation of observations of cold molecular cores. Three papers are concerned with astrophysical turbulence in differentially rotating systems. One paper focuses on the development of a GPU-based computational method useful for such turbulence models. One paper looks into the observational validation of the turbulence models with the help of radiative transfer simulations. In that sense, this work does not deal with just a single tool or methodology but has been a part of a dialogue between astrophysicists working with turbulence (both in galaxies and in Sun-like stars), astronomers working with the cold ISM and computer scientists dealing with HPC. Therefore, both results and future prospects are divided into various threads.

Based on our results, Ophiuchus D and Chamaeleon-MMS1 have manifested rich dynamical structures; the full understanding of which is still lacking. Especially Chamaeleon-MMS1 being a candidate for a rarely seen early stage of star formation, begs for a deeper look: It shows an unusual velocity structure, with potential inflow and outflow features, and dynamical influence from its neighbour.

These small-scale dynamical structures could be explored more closely with high-resolution observations by ALMA, giving more detail to several unresolved issues. Also an MHD model of a molecular outflow colliding with a cloud would give insights on the little-known interaction with prestellar objects. Lastly, better MHD models exploring the effect of turbulence on molecular clouds could inform the origin and formation of such cores.

In our studies of MRI turbulence, we have argued that MRI can either be weakened or dampened by an outside source of turbulence. We have also shown support to the notion that SNe generate vortical turbulent flow due to baroclinicity and that small-scale flows can generate large-scale flows by the AKA-affect. Parametrization of the complicated chain of a multitude of processes should yet be pursued for, but on the other hand it may be too challenging a task.

Therefore, it is important to look for other avenues to advance the modelling frontier. All models are simplification of the real system, and only by gradual improvements, incrementally adding more physics, can one identify the importance of various effects. Evidently, MHD turbulence models can be improved with higher resolution allowed by increasing computational capabilities. However, there are more creative approaches to

the challenge. One of them is to refine a part of the turbulence model into smaller scales, approaching the length scales of cold cores. This would require methods for scaling down from larger simulations without introducing artefacts through boundary conditions, including self-gravity and adapting a more refined cooling model for $T < 100$ K. Another interesting path of investigation would be to produce full MHD versions of the fast-rotating *Paper VII* models to observe the potential emergence of MRI within SNe turbulence.

We also simulated polarization based on SN-dynamo model data, which in particular allowed us to study the effects of the diffuse hot component, and also the role of SN shocks. We found that we observe comparable behaviour as mapped by the Planck satellite. Especially, we found that our model could produce comparable filamentary structures in polarization angle dispersion $\mathcal{S}$, as was shown by Planck Collaboration Int. XIX (2015). In this way the results can illuminate the role of diffuse ISM in the Planck polarization maps and that there is a potential avenue for testing the applicability of SN-driven dynamo-active DNS models to the Milky Way galaxy. *Paper VI* present the preliminary results of this study.

Even the current models offer further possibilities for improved and more detailed analysis for a later time point. The relationship between magnetic field as polarization angle dispersion can be examined in more detail, in connection the Chandrasekhar-Fermi method used to estimate the strength of a magnetic field based on polarization angles (Chandrasekhar & Fermi, 1953; Hildebrand et al., 2009). This way it could be possible to calculate better estimates of the galactic mean field. Another possibility would be to look pole-ward and make analysis comparable to Planck Collaboration Int. XLIV (2016) to see how magnetic field structure affects such observational estimates. In addition, with improved dynamo models, with improved resolution and/or new physical effects, the developed analysis tools can be utilized to produce new comparisons with observations.

We have produced a working proof-of-concept code Astaroth which efficiently performs high-order FDM computations on a single GPU. Development on Astaroth is an ongoing process. At the moment, it is being improved in two ways. First is to add more functionalities, essentially to be able to handle the full set of MHD equations. Second is to parallelize the system for multi-GPU setup, after which massively parallel applications of the code become possible. Especially with improved range of physical effects, Astaroth can become a testbed for new ideas, even before massive multi-GPU systems are available.

The work presented in this thesis has been motivated by the will to maintain a dialogue between different domains of specialization. Although we focus on specific features and interpretations, the ISM is by no means a less complex phenomenon than the evolution of the Earth climate over millions of years. The central processes merely take more time, much more than the cosmically insignificant lifespan of a single human life. To us, what is a dramatically violent and chaotic process, just appears to stand still.

Bibliography

Abbott, D. C. 1982, The Astrophysical Journal, 263, 723

ALMA Partnership, Asayama, S., Biggs, A., et al. 2016, ALMA Cycle 4 Technical Handbook, ISBN 978-3-319-08941-6

Alves de Oliveira, C., Schneider, N., Merín, B., et al. 2014, Astronomy & Astrophysics, 568, A98

Andersson, B.-G., Lazarian, A., & Vaillancourt, J. E. 2015, Annual Review of Astronomy & Astrophysics, 53, 501

Andre, P., Ward-Thompson, D., & Barsony, M. 2000, Protostars and Planets IV, 59

Arce, H. G., & Sargent, A. I. 2006, The Astrophysical Journal, 646, 1070

Armstrong, J. W., Cordes, J. M., & Rickett, B. J. 1981, Nature, 291, 561

Armstrong, J. W., Rickett, B. J., & Spangler, S. R. 1995, The Astrophysical Journal, 443, 209

Bachiller, R., Martin-Pintado, J., & Fuente, A. 1991, Astronomy & Astrophysics, 243, L21

—. 1993, The Astrophysical Journal Letters, 417, L45

Balbus, S. A. 2003, Annual Review of Astronomy & Astrophysics, 41, 555

Balbus, S. A., & Hawley, J. F. 1991, The Astrophysical Journal, 376, 214

—. 1998, Reviews of Modern Physics, 70, 1

Balsara, D., & Pouquet, A. 1999, Physics of Plasmas, 6, 89

Balsara, D. S., & Dumbser, M. 2015, Journal of Computational Physics, 287, 269

Balsara, D. S., Kim, J., Mac Low, M.-M., & Mathews, G. J. 2004, The Astrophysical Journal, 617, 339

Barsony, M. 1994, in Astronomical Society of the Pacific Conference Series, Vol. 65, Clouds, Cores, and Low Mass Stars, ed. D. P. Clemens & R. Barvainis, 197

Baryshev, A. M., Hesper, R., Mena, F. P., et al. 2015, Astronomy & Astrophysics, 577, A129

Beck, R. 2016, The Astronomy and Astrophysics Review, 24, 4

Beck, R., Brandenburg, A., Moss, D., Shukurov, A., & Sokoloff, D. 1996, Annual Review of Astronomy & Astrophysics, 34, 155

Belloche, A., Parise, B., van der Tak, F. F. S., et al. 2006, Astronomy & Astrophysics, 454, L51

Bendre, A., Gressel, O., & Elstner, D. 2015, Astronomische Nachrichten, 336, 991

Bergin, E. A., & Tafalla, M. 2007, Annual Review of Astronomy & Astrophysics, 45, 339

Blandford, R. D., & Payne, D. G. 1982, Monthly Notices of the Royal Astronomical Society, 199, 883

Bonnor, W. B. 1956, Monthly Notices of the Royal Astronomical Society, 116, 351

Bournaud, F., Elmegreen, B. G., Teyssier, R., Block, D. L., & Puerari, I. 2010, Monthly Notices of the Royal Astronomical Society, 409, 1088

Brandenburg, A. 2001, The Astrophysical Journal, 550, 824

—. 2003, Computational aspects of astrophysical MHD and turbulence, Advances in Nonlinear Dynamics, ed. A. Ferriz-Mas & M. Núñez, 269

Brandenburg, A., Korpi, M. J., & Mee, A. J. 2007, The Astrophysical Journal, 654, 945

Brandenburg, A., Nordlund, A., Stein, R. F., & Torkelsson, U. 1995, The Astrophysical Journal, 446, 741

Brandenburg, A., & Rekowski, B. V. 2001, Astronomy & Astrophysics, 379, 1153

Bregman, J. N. 1980, The Astrophysical Journal, 236, 577

Caunt, S. E., & Korpi, M. J. 2001, Astronomy and Astrophysics, 369, 706

Chandrasekhar, S. 1960, Proceedings of the National Academy of Science, 46, 253

—. 1961, Hydrodynamic and hydromagnetic stability, International Series of Monographs on Physics, Oxford: Clarendon

Chandrasekhar, S., & Fermi, E. 1953, The Astrophysical Journal, 118, 113

Chernin, A. D. 1996, Vistas in Astronomy, 40, 257

Chevalier, R. A. 1977, Annual Review of Astronomy & Astrophysics, 15, 175

Chini, R., Reipurth, B., Sievers, A., et al. 1997, Astronomy & Astrophysics, 325, 542

Courant, R., Friedrichs, K., & Lewy, H. 1928, Mathematische Annalen, 100, 32

Cox, D. P., & Smith, B. W. 1974, The Astrophysical Journal Letters, 189, L105

CSC. 2017, Taito User Guide, CSC - IT Center for Science Ltd., [Online]. Available: `https://research.csc.fi/taito-user-guide/`. Referenced: 25.4.2017

Davis, C. J., & Eisloeffel, J. 1995, Astronomy & Astrophysics, 300, 851

Davis, Jr., L., & Greenstein, J. L. 1951, The Astrophysical Journal, 114, 206

de Plancy, J. C. 1863, Dictionnaire infernal (Henri Plon, Paris)

Dib, S., Bell, E., & Burkert, A. 2006, The Astrophysical Journal, 638, 797

Dobler, W., Stix, M., & Brandenburg, A. 2006, The Astrophysical Journal, 638, 336

Dolginov, A. Z., & Mytrophanov, I. G. 1976, Astrophysics and Space Science, 43, 257

Draine, B. T. 2003, Annual Review of Astronomy & Astrophysics, 41, 241

Draine, B. T., & Weingartner, J. C. 1996, The Astrophysical Journal, 470, 551

Dunham, M. M., Chen, X., Arce, H. G., et al. 2011, The Astrophysical Journal, 742, 1

Ebert, R. 1955, Zeitschrift für Astrophysik, 37, 217

Elmegreen, B. G. 2011, The Astrophysical Journal, 737, 10

Elmegreen, B. G., & Scalo, J. 2004, Annual Review of Astronomy & Astrophysics, 42, 211

Federrath, C., Sur, S., Schleicher, D. R. G., Banerjee, R., & Klessen, R. S. 2011, The Astrophysical Journal, 731, 62

Ferrière, K. 1996, Astronomy & Astrophysics, 310, 438

Ferrière, K. M. 2001, Reviews of Modern Physics, 73, 1031

Fiege, J. D., & Pudritz, R. E. 2000, The Astrophysical Journal, 544, 830

Field, G. B., Goldsmith, D. W., & Habing, H. J. 1969, The Astrophysical Journal Letters, 155, L149

Gaustad, J. E., McCullough, P. R., Rosing, W., & Van Buren, D. 2001, The Publications of the Astronomical Society of the Pacific, 113, 1326

Gent, F. A., Shukurov, A., Fletcher, A., Sarson, G. R., & Mantere, M. J. 2013a, Monthly Notices of the Royal Astronomical Society, 432, 1396

Gent, F. A., Shukurov, A., Sarson, G. R., Fletcher, A., & Mantere, M. J. 2013b, Monthly Notices of the Royal Astronomical Society, 430, L40

Goldreich, P., & Kylafis, N. D. 1981, The Astrophysical Journal Letters, 243, L75

—. 1982, The Astrophysical Journal, 253, 606

Górski, K. M., Hivon, E., Banday, A. J., et al. 2005, The Astrophysical Journal, 622, 759

Gottlieb, D., & Hesthaven, J. S. 2001, Journal of Computational and Applied Mathematics, 128, 83

Gressel, O., Elstner, D., & Ziegler, U. 2013, Astronomy & Astrophysics, 560, A93

Gressel, O., Elstner, D., Ziegler, U., & Rüdiger, G. 2008, Astronomy & Astrophysics, 486, L35

Gropp, W., Lusk, E., Doss, N., & Skjellum, A. 1996, Parallel Computing, 22, 789–828

Hanasz, M., Otmianowska-Mazur, K., & Lesch, H. 2002, Astronomy & Astrophysics, 386, 347

Hansen, S. S. 1982, The Astrophysical Journal, 260, 599

Haugen, N. E. L., Brandenburg, A., & Mee, A. J. 2004, Monthly Notices of the Royal Astronomical Society, 353, 947

Hawley, J. F., & Balbus, S. A. 1991, The Astrophysical Journal, 376, 223

Hawley, J. F., Gammie, C. F., & Balbus, S. A. 1995, The Astrophysical Journal, 440, 742

Hayashi, M. R., Shibata, K., & Matsumoto, R. 1996, The Astrophysical Journal Letters, 468, L37

Heinemann, T., & Papaloizou, J. C. B. 2009, Monthly Notices of the Royal Astronomical Society, 397, 64

Hester, J. J., Scowen, P. A., Sankrit, R., et al. 1996, The Astronomical Journal, 111, 2349

Heyer, M., & Dame, T. M. 2015, Annual Review of Astronomy & Astrophysics, 53, 583

Hildebrand, R. H., Kirby, L., Dotson, J. L., Houde, M., & Vaillancourt, J. E. 2009, The Astrophysical Journal, 696, 567

Hiramatsu, M., Hayakawa, T., Tatematsu, K., et al. 2007, The Astrophysical Journal, 664, 964

Hirshman, S. P., & Whitson, J. C. 1983, Physics of Fluids, 26, 3553

Ho, P. T. P., & Townes, C. H. 1983, Annual Review of Astronomy & Astrophysics, 21, 239

Holland, W. S., Bintley, D., Chapin, E. L., et al. 2013, Monthly Notices of the Royal Astronomical Society, 430, 2513

Ibáñez-Mejía, J. C., Mac Low, M.-M., Klessen, R. S., & Baczynski, C. 2016, The Astrophysical Journal, 824, 41

Iffrig, O., & Hennebelle, P. 2017, Astronomy & Astrophysics, 604, A70

Iroshnikov, P. S. 1964, Soviet Astronomy, 7, 566

Jin, L. 1996, The Astrophysical Journal, 457, 798

Jones, T. J., Klebe, D., & Dickey, J. M. 1992, The Astrophysical Journal, 389, 602

Joos, M., Hennebelle, P., Ciardi, A., & Fromang, S. 2013, Astronomy & Astrophysics, 554, A17

Ju, W., Stone, J. M., & Zhu, Z. 2017, The Astrophysical Journal, 841, 29

Juvela, M. 2005, Astronomy & Astrophysics, 440, 531

Juvela, M., Ristorcelli, I., Pelkonen, V.-M., et al. 2011, Astronomy & Astrophysics, 527, A111

Käppeli, R., & Mishra, S. 2016, Astronomy & Astrophysics, 587, A94

Kerzendorf, W. E., & Sim, S. A. 2014, Monthly Notices of the Royal Astronomical Society, 440, 387

Khokhlov, A., Mueller, E., & Hoeflich, P. 1993, Astronomy & Astrophysics, 270, 223

Korpi, M., Brandenburg, A., Shukurov, A., & Tuominen, I. 1999a, in Interstellar Turbulence, ed. J. Franco & A. Carraminana, 127

Korpi, M. J. 1999, PhD thesis, OULUN YLIOPISTO (FINLAND)

Korpi, M. J., Brandenburg, A., Shukurov, A., & Tuominen, I. 1999b, Astronomy & Astrophysics, 350, 230

Korpi, M. J., Brandenburg, A., Shukurov, A., Tuominen, I., & Nordlund, Å. 1999c, The Astrophysical Journal Letters, 514, L99

Kraichnan, R. H. 1965, Physics of Fluids, 8, 1385

Lada, C. J. 1985, Annual Review of Astronomy & Astrophysics, 23, 267

Ladd, E. F., Wong, T., Bourke, T. L., & Thompson, K. L. 2011, The Astrophysical Journal, 743, 108

Larson, R. B. 1969, Monthly Notices of the Royal Astronomical Society, 145, 271

Lax, P. D., & Richtmyer, R. D. 1956, Communications on Pure and Applied Mathematics, 9, 267

Li, Z.-Y., Krasnopolsky, R., Shang, H., & Zhao, B. 2014, The Astrophysical Journal, 793, 130

Lodders, K. 2003, The Astrophysical Journal, 591, 1220

Lombardi, M., Lada, C. J., & Alves, J. 2008, Astronomy & Astrophysics, 480, 785

Lunttila, T., Padoan, P., Juvela, M., & Nordlund, Å. 2009, The Astrophysical Journal Letters, 702, L37

Mac Low, M.-M. 1999, The Astrophysical Journal, 524, 169

Machida, M. N., Inutsuka, S.-i., & Matsumoto, T. 2008, The Astrophysical Journal, 676, 1088

Machida, M. N., Matsumoto, T., & Inutsuka, S.-i. 2016, Monthly Notices of the Royal Astronomical Society, 463, 4246

Mäkelä, M. M., & Haikala, L. K. 2013, Astronomy & Astrophysics, 550, A83

Malinen, J., Montier, L., Montillaud, J., et al. 2016, Monthly Notices of the Royal Astronomical Society, 460, 1934

Mantere, M. J., & Cole, E. 2012, The Astrophysical Journal, 753, 32

Mathis, J. S., Mezger, P. G., & Panagia, N. 1983, Astronomy & Astrophysics, 128, 212

Matsumoto, T., Machida, M. N., & Inutsuka, S.-i. 2017, The Astrophysical Journal, 839, 69

Maureira, M. J., Arce, H. G., Dunham, M. M., et al. 2017, The Astrophysical Journal, 838, 60

McKee, C. F., & Ostriker, E. C. 2007, Annual Review of Astronomy & Astrophysics, 45, 565

McKee, C. F., & Ostriker, J. P. 1977, The Astrophysical Journal, 218, 148

Meneguzzi, M., Frisch, U., & Pouquet, A. 1981, Physical Review Letters, 47, 1060

Mittal, S., & Vetter, J. S. 2014, ACM Comput. Surv., 47, 19:1

Motte, F., Andre, P., & Neri, R. 1998, Astronomy & Astrophysics, 336, 150

Murray, N. 2011, The Astrophysical Journal, 729, 133

NVIDIA. 2017, CUDA Toolkit Documentation, NVIDIA, [Online]. Available: `http://docs.nvidia.com/cuda/index.html`. Referenced: 1.5.2017

Offner, S. S. R., Dunham, M. M., Lee, K. I., Arce, H. G., & Fielding, D. B. 2016, The Astrophysical Journal Letters, 827, L11

Ostriker, J. P., & McKee, C. F. 1988, Reviews of Modern Physics, 60, 1

Padoan, P., Haugbølle, T., Nordlund, Å., & Frimann, S. 2017, The Astrophysical Journal, 840, 48

Padoan, P., Juvela, M., Pan, L., Haugbølle, T., & Nordlund, Å. 2016a, The Astrophysical Journal, 826, 140

Padoan, P., Pan, L., Haugbølle, T., & Nordlund, Å. 2016b, The Astrophysical Journal, 822, 11

Palmeirim, P., André, P., Kirk, J., et al. 2013, Astronomy & Astrophysics, 550, A38

Pan, L., Padoan, P., Haugbølle, T., & Nordlund, Å. 2016, The Astrophysical Journal, 825, 30

Parker, E. N. 1992, The Astrophysical Journal, 401, 137

Parkin, T. J., Wilson, C. D., Foyle, K., et al. 2012, Monthly Notices of the Royal Astronomical Society, 422, 2291

Parmar, P. S., Lacy, J. H., & Achtermann, J. M. 1991, The Astrophysical Journal Letters, 372, L25

Pelkonen, V.-M., Juvela, M., & Padoan, P. 2009, Astronomy & Astrophysics, 502, 833

Pencil Code User's Manual. 2017, The Pencil Code: A High-Order MPI Code for MHD Turbulence. User's and Reference Manual, NORDITA, [Online]. Available: `http://pencil-code.nordita.org/doc/manual.pdf`. Referenced: 25.4.2017

Planck Collaboration Int. L. 2017, Astronomy & Astrophysics, 599, A51

Planck Collaboration Int. XIX. 2015, Astronomy & Astrophysics, 576, A104

Planck Collaboration Int. XLII. 2016, Astronomy & Astrophysics, 596, A103

Planck Collaboration Int. XLIV. 2016, Astronomy & Astrophysics, 596, A105

Planck Collaboration Int. XX. 2015, Astronomy & Astrophysics, 576, A105

Planck Collaboration Int. XXXII. 2016, Astronomy & Astrophysics, 586, A135

Planck Collaboration Int. XXXIII. 2016, Astronomy & Astrophysics, 586, A136

Planck Collaboration XI. 2014, Astronomy & Astrophysics, 571, A11

Rädler, K. 1980, Astronomische Nachrichten, 301, 101

Reiter, M., Kiminki, M. M., Smith, N., & Bally, J. 2017, Monthly Notices of the Royal Astronomical Society, 467, 4441

Schneider, N., Csengeri, T., Bontemps, S., et al. 2010, Astronomy & Astrophysics, 520, A49

Seifried, D., Sánchez-Monge, Á., Walch, S., & Banerjee, R. 2016, Monthly Notices of the Royal Astronomical Society, 459, 1892

Sellwood, J. A., & Balbus, S. A. 1999, The Astrophysical Journal, 511, 660

Shakura, N. I., & Sunyaev, R. A. 1973, Astronomy & Astrophysics, 24, 337

Shibata, K. and Matsumoto, R. 1991, Nature, 353, 633, 10.1038/353633a0

Shu, F., Najita, J., Ostriker, E., et al. 1994, The Astrophysical Journal, 429, 781

Shu, F. H., Najita, J. R., Shang, H., & Li, Z.-Y. 2000, Protostars and Planets IV, 789

Sipilä, O. 2013, PhD thesis, University of Helsinki, Department of Physics, `http://urn.fi/URN:ISBN:978-952-10-8945-9`

Sipilä, O., Harju, J., & Juvela, M. 2011, Astronomy & Astrophysics, 535, A49

Soler, J. D., Hennebelle, P., Martin, P. G., et al. 2013, The Astrophysical Journal, 774, 128

Soler, J. D., Alves, F., Boulanger, F., et al. 2016, Astronomy & Astrophysics, 596, A93

Stanescu, D., & Habashi, W. 1998, Journal of Computational Physics, 143, 674

Steenbeck, M., Krause, F., & Rädler, K.-H. 1966, Zeitschrift Naturforschung Teil A, 21, 369

Steinacker, J., Baes, M., & Gordon, K. D. 2013, Annual Review of Astronomy & Astrophysics, 51, 63

Sur, S., Schleicher, D. R. G., Banerjee, R., Federrath, C., & Klessen, R. S. 2010, The Astrophysical Journal Letters, 721, L134

Suutarinen, A. N., Kristensen, L. E., Mottram, J. C., Fraser, H. J., & van Dishoeck, E. F. 2014, Monthly Notices of the Royal Astronomical Society, 440, 1844

Tafalla, M., Santiago-García, J., Myers, P. C., et al. 2006, Astronomy & Astrophysics, 455, 577

Tobin, J. J., Hartmann, L., Bergin, E., et al. 2012, The Astrophysical Journal, 748, 16

Tobin, J. J., Hartmann, L., Looney, L. W., & Chiang, H.-F. 2010, The Astrophysical Journal, 712, 1010

Tobin, J. J., Hartmann, L., Chiang, H.-F., et al. 2011, The Astrophysical Journal, 740, 45

Tóth, G. 2000, Journal of Computational Physics, 161, 605

van Dishoeck, E. F., & Blake, G. A. 1998, Annual Review of Astronomy & Astrophysics, 36, 317

Vazquez-Semadeni, E., Passot, T., & Pouquet, A. 1995, The Astrophysical Journal, 441, 702

Velikhov, E. P. 1959, Soviet Physics JETP, 36, 995

von Alfthan, S., Pokhotelov, D., Kempf, Y., et al. 2014, Journal of Atmospheric and Solar-Terrestrial Physics, 120, 24

Von Neumann, J., & Richtmyer, R. D. 1950, Journal of Applied Physics, 21, 232

Ward-Thompson, D., Kirk, J. M., Crutcher, R. M., et al. 2000, The Astrophysical Journal Letters, 537, L135

Weyer, J. 1568, De praestigiis daemonum (Oporinus)

Whittet, D. C. B., Prusti, T., Franco, G. A. P., et al. 1997, Astronomy & Astrophysics, 327, 1194

Wolfire, M. G., Hollenbach, D., McKee, C. F., Tielens, A. G. G. M., & Bakes, E. L. O. 1995, The Astrophysical Journal, 443, 152

Workman, J. C., & Armitage, P. J. 2008, The Astrophysical Journal, 685, 406

Ziegler, U. 2008, Computer Physics Communications, 179, 227

Zubko, V., Dwek, E., & Arendt, R. G. 2004, The Astrophysical Journal Supplement Series, 152, 211